ADVANCED FUNCTIONAL MATERIALS
www.afm-journal.de

High-Performance $NiCo_2O_4$/Graphene Quantum Dots for Asymmetric and Symmetric Supercapacitors with Enhanced Energy Efficiency

*Ambadi Lakshmi-Narayana, Navid Attarzadeh, Vaithalingam Shutthanandan, and Chintalapalle V. Ramana**

For the sustainable growth of future generations, energy storage technologies like supercapacitors and batteries are becoming more and more common. However, reliable and high-performance materials' design and development is the key for the widespread adoption of batteries and supercapacitors. Quantum dots with fascinating and unusual properties are expected to revolutionize future technologies. However, while the recent discovery of quantum dots honored with a Nobel prize in Chemistry, their benefits for the tenacious problem of energy are not realized yet. In this context, herein, chemical-composition tuning enabled exceptional performance of $NiCo_2O_4$(NCO)/graphene quantum dots (GQDs) is reported, which outperform the existing similar materials, in supercapacitors. A comprehensive study is performed on the synthesis, characterization, and electrochemical performance evaluation of highly functional NCO/GQDs in supercapacitors delivering enhanced energy efficiency. The high-performance, functional NCO/GQDs electrode materials are synthesized by the incorporation of GQDs into NCO. The effect of variable amount of GQDs on the energy performance characteristics of NCO/GQDs in supercapacitors is studied systematically. In-depth structural and chemical bonding analyses using X-ray diffraction (XRD) and Raman spectroscopic studies indicate that all the NCO/GQDs composites crystallize in the spinel cubic phase of $NiCo_2O_4$ while graphene integration evident in all the NCO/GQDs. The scanning electron microscopy imaging analysis reveals homogeneously distributed spherical particles with a size distribution of 5–9 nm validating the formation of QDs. The high-resolution transmission electron microscopy analyses reveal that the NCOQDs are anchored on graphene sheets, which provide a high surface area of 42.27 m^2g^{-1} and high mesoporosity for the composition of NCO/GQDs-10%. In addition to establishing reliable electrical connection to graphene sheets, the NCOQDs provide reliable 3D-conductive channels for rapid transport throughout the electrode as well as synergistic effects. Chemical-composition tuning, and optimization yields NCO/GQDs-10% to deliver the best specific capacitance of 3940 Fg^{-1} at 0.5 Ag^{-1}, where the electrodes retain ≈98% capacitance after 5000 cycles. The NCO/GQD-10%//AC asymmetric supercapacitor device demonstrates outstanding energy density and power density values of 118.04 Wh kg^{-1} and 798.76 W kg^{-1}, respectively. The NCO/GQDs-10%//NCO/GQDs-10% symmetric supercapacitor device delivers excellent energy and power density of 24.30 Wh kg^{-1} and 500 W kg^{-1}, respectively. These results demonstrate and conclude that NCO/GQDs are exceptional and prospective candidates for developing next-generation high-performance and sustainable energy storage devices.

A. Lakshmi-Narayana, N. Attarzadeh, C. V. Ramana
Center for Advanced Materials Research (CMR)
University of Texas at El Paso
500 W University Ave, El Paso, TX 79968, USA
E-mail: rvchintalapalle@utep.edu

The ORCID identification number(s) for the author(s) of this article can be found under https://doi.org/10.1002/adfm.202316379

DOI: 10.1002/adfm.202316379

A. Lakshmi-Narayana, V. Shutthanandan, C. V. Ramana
Department of Aerospace & Mechanical Engineering
University of Texas at El Paso
500 W. University Ave., El Paso, TX 79968, USA

N. Attarzadeh, V. Shutthanandan
Environmental Science and Engineering
University of Texas at El Paso
500 W. University Ave., El Paso, TX 79968, USA

V. Shutthanandan
Environmental Molecular Sciences Laboratory (EMSL)
Pacific Northwest National Laboratory (PNNL)
Richland, WA 99352, USA

1. Introduction

One of the major, global issues is the continually raising demand for energy and the depletion of fossil fuels. In addition, using fossil fuels in a wide variety of domestic, industrial, and transportation sectors produces greenhouse gases, which causes environmental pollution and global warming. In this context, development of economically viable and ecofriendly energy technologies is the key to tackling greenhouse effect and environment pollution and secure eco-balance and sustainability for future generations.[1–3] Furthermore, in recent years, continuously thriving interest in hybrid vehicles (HEVs) and portable electronic devices (PEDs) created a seemingly insistent demand for energy storage that divulged great challenges toward the amplification of electrochemical performance.[4] Specifically, significant attention directed toward the design and development of various electrochemical energy storage (EES) systems with the desirable properties and performance characteristics of high-power density, high energy density, and extended service life.

The two most exciting and widespread energy storage devices are Lithium (Li) – ion batteries (LIBs) and supercapacitors (SCs).[5] LIBs received extensive interest due to their high energy/gravimetric densities of <250 Whkg^{-1} and volumetric energy densities of <650 WhL^{-1}. The large volume change during charge–discharge process, low Li-diffusivity, low mechanical stability causes pulverization and causes poor cycliability, rate capability as well as lesser power density. Whereas SCs are promising charge-storage devices with incredible beneficial characteristics, such as large specific capacitance (C_s) and short discharge time of 1–10s for SCs versus 10–60 min for LIBs. High power performance (10 kW kg^{-1}) in a short duration is possible with SCs. Furthermore, SCs offer long cycle life of >30 000 versus >1000 cycles for LIBs, rapid charge–discharge rate with environmentally friendliness as well as bridging the energy gaps between batteries and classical dielectric capacitors.[6] Based on the charge storage mechanism, there are three types of SCs: i) electrical double layer capacitors (EDLCs), ii) pseudocapacitors, and iii) hybrid capacitors. Carbon-based nanostructured materials, such as carbon (C), SWCNTs, MWCNT, and graphene etc., were employed as electrode materials in EDLCs due to their excellent surface area and high conductivity.[7,8] In pseudocapacitors, faradaic charge transfer takes place between the electrolyte and the (sub)surface of a suitable metal oxide or hydroxide electrode by a reversible redox reaction, electrode sorption/desorption, or an intercalation process.[9] Hybrid capacitor contains both positive electrode (positrode) and negative electrode (negatrode). The EDLC capacitive mechanism is provided by negatrode and contains high power density whereas positrode facilitates pseudocapacitive nature with high energy density. The best features of EDLCs and pseudocapacitive electrodes make the hybrid capacitor with high specific capacitance, high energy density, high power density, and wider working potential window.[10] Conducting plymers, such as olyaniline (PANI), poly(3,4–ethylene-dioxythiophene) (PEDOT), polypyrrole (PPy), polythiophene (PTh), polyphenylene vinylene (PPV), polyindole (PIN),[11–13] and metal oxides can be used as electrode materials for pseudocapacitors. Conducting polymers are good in storing the charge in pseudocapacitors. Nevertheless, their poor cyclic stability due to volume expansion hindered the practical usage, in contrast to metal oxides, in capacitor device applications.

Various metal oxides and metal hydroxides such as RuO_2, MnO_2, NiO, Co_3O_4, MoO_3, $LiMn_2O_4$, $Ni(OH)_2$, $Mn(OH)_2$, $Fe(OH)_2$, $Co(OH)_2$, V_2O_5, Li_2TiO_3 were used as pseudocapacitive materials due to their high theoretical specific capacitance and good structural stability.[14–19] RuO_2 is a well-established electrode material for SCs because of its high theoretical specific capacitance (C_s = >2000 Fg^{-1}), reversible charge/discharge characteristics, and good electrical conductivity. However, the high cost and toxic nature impedes its widespread usage in practical device applications. The scientific and research community switched attention to binary metal oxides due to the sluggish kinetics of electrons/ions between the electrode and the electrolyte of mono metal-oxides.[20,21] Unlike monometal oxides, binary transition metal oxides are promising electrode materials for SCs. The binary metal oxides are in the cubic spinel structure, which can be represented by the chemical formula AB_2O_4, where cation sites (A: tetrahedral, B: octahedral) are occupied by 3D transition metals. The better electrical conductivity and rich redox chemistry of these oxides are the result of the synergistic interaction of metal cations.

Among the spinel structured metal oxides considered for SCs, $NiCo_2O_4$ (NCO) with a high theoretical specific capacitance (3000 Fg^{-1}) is a promising electrode material. In comparison to respective mono metals (Ni and Co) and mono metal oxides (NiO and Co_3O_4), NCO has received the greatest attention because of its superior electrical conductivity, higher electrochemical activity, strong redox activity, tremendous flexibility, low cost, and abundance in nature.[22] The NCO spinel contains multiple redox states and is a *p*-type semiconductor with a bandgap of 2.1 eV. The electronic conductivity of NCO is often explained in terms of band structure by means of intervening oxygen ion through a strong covalent interaction between low spin Co^{3+}-Ni^{3+} in octahedral site assuming the distribution $Co^{2+}(Ni^{3+}\ Co^{3+})\ O_4$.[23,24] In the context of realizing SCs with superior performance, integrating NCO with carbonaceous composite structure is an effective approach. NCO/C composites specifically offer advantages to overcome low specific capacitance and narrow potential window, and they enhance the energy density, cycle life, and power density.[25] These carbon-based composite materials not only improve the electrical conductivity but also enhance the surface area and surface wettability. Moreover, the practical capacitance in metal oxides is typically less than theoretical values due to larger particle size. Composites formed by the integration of oxide with C-based materials readily induce reduction of the particle-size to the quantum dot (nano) range, which is expected to enhance the specific capacitance and rate capability due to shortening the path length that ions and electrons passes through the electrolyte and reach the surface of the particles.[26–28]

The present work was performed on NCO integrated with graphene quantum dots (GQDs) (see, **Figure 1a**) for application in SCs. Due to their ultra-small size (4–10 nm), quantum dots allow large specific surface area and can dramatically enhance the SCs' performance by shortening their diffusion lengths. The

C. V. Ramana
Physical and Computational Sciences Directorate (PCSD)
Pacific Northwest National Laboratory (PNNL)
Richland, WA 99352, USA

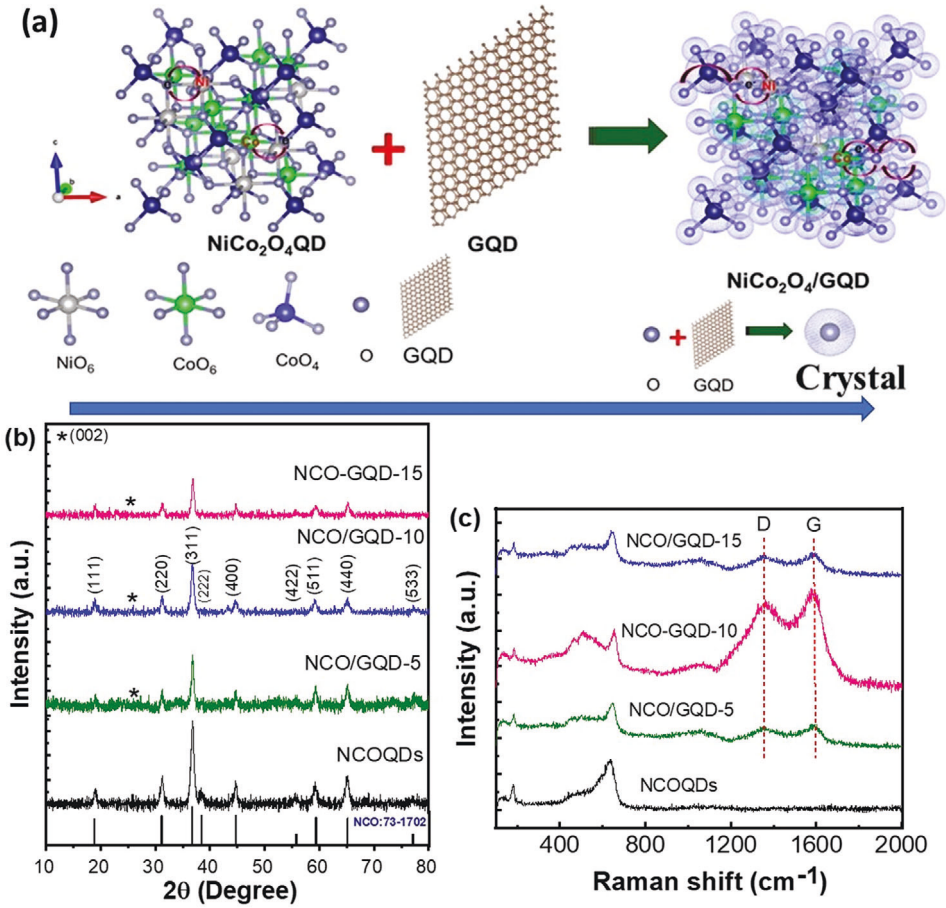

Figure 1. a) Schematic illustration of formation of $NiCo_2O_4$/GQDs. b) XRD patterns of pristine NCOQDs and NCO/GQDs with different weight percentages (5%,10%, and 15%) of GQDs. The indexing of the peaks is as shown in the figure. The experimental XRD patterns are compared with pure $NiCo_2O_4$ (PDF-73-1702). All the peaks observed are due to NCO, while (002) peak indicated with a symbol * is due to graphene. c) Raman spectra of pristine NCOQDs and NCO/GQDs with variable GQD content. The presence of D and G bands confirm the formation of NCO/GQDs.

improved surface wettability of composite electrodes with QDs integrated also contributes to the enhanced pseudocapacitance.[29–31] However, when it comes to NCO/GQDs composites, only a few reports that too with limited scope exist. Also, the effect of variable concentration of GQDs in NCO/GQDs composite electrodes and their chemical tuning for applications in SCs was rarely reported. Poonam et al. synthesized NCO-QDs at 300 °C by simple hydrothermal method to obtain 3D flower-like NCO structures, which delivered a C_s of 362 Fg^{-1} (at a current density of 0.5 A g^{-1}). Carbon QDs tuned porous NCO composites prepared using reflux synthesis exhibit high-specific capacitance of 856 Fg^{-1} at 1 Ag^{-1} and excellent rate capability (83.9%, 72.5%, and 60.8% capacity retention rate at 20, 50, and 100 Ag^{-1}, respectively.[32]) However, post-processing annealing was needed to obtain these characteristics. Nanocomposites of reduced graphene oxide (rGO) and NCO made by hydrothermal method delivered a C_s of 265 Fg^{-1} (at 0.73 Ag^{-1}).[33] Yin et al. designed multi-layer NiO@Co_3O_4 hollow sphere decorated with GQDs via solvothermal route and applied for LIBs and SCs. The NiO@Co_3O_4 @ GQDs delivered a good C_s of 1361 Fg^{-1} at 1 Ag^{-1} and retained ≈77% capacitance after 3000 cycles.[34] The nanocomposite with hierarchical mesoporous NCO nano needle array on carbon cloth was fabricated using a hydrothermal route by Zhang et al. The newly fabricated carbonaceous composite delivered a good C_s of 660 Fg^{-1} at 2 Ag^{-1} with a good cyclic stability of 91.8% after 3000 cycles.[35] Prashant et al. fabricated surface modified Ni wire/NCO/rGO (Ni/NCO/rGO) electrode by a combination of solvothermal and hydrothermal deposition methods.[23] Ni_{10}/NCO/rGO electrode delivered a volumetric specific capacitance of 253 F cm^{-3} with good structural stability.[36] Li et al. synthesized carbon nanosphere (CNS)/NCO core shell sub microspheres by hydrothermal method followed by a thermal treatment at 350 °C for 2 h. These specially designed CNS/NCO core shell sub microspheres achieved a C_s of 1420 Fg^{-1} at 1 Ag^{-1} and holds 98.5% capacitance retention after 3000 cycle.[37] Nguyen et al. reported that the C/NCO nanocomposite was synthesized by hydrothermal method and delivered a specific capacitance of 204.28 Fg^{-1} at 1 Ag^{-1}. It holds C_s retention of 90.35% of initial C_s after 3000 cycles.[38] A NCO nanoparticles/3D porous graphene ($NiCO_2O_4$/3D-G) composite was synthesized by a hydrothermal method combined with subsequent annealing treatment. 3D–porous graphene special structure with the cross-linked network offers excellent conductivity and ion/electron transport. As a result NCO/3D-G

composite demonstrated a good C_s value of 1588 Fg^{-1} at 1 Ag^{-1}.[39] The NCO nanorods anchored on CNFs formed as NCO@CNFS composites provide high surface area and facilitate high conductivity due to the synergistic effect.[40] As a result, this NCO@CNFS composite delivered a C_s of 649 Fg^{-1} at 3 Ag^{-1} with good structural stability.[40] Jiang et al. presented an NCO/rGO hybrid nanostructure, and it has been constructed on carbon fibers (NCO/rGO/CF) via a hydrothermal route. In addition to rGO, the hierarchical porous structure of NCO nanowires with synergistic effect the NCO/rGO/CF provides high surface area and good electrical conductivity as a result it delivered C_s of 931 Fg^{-1} at 1 Ag^{-1} with good cycliability.[41] Luo et al.[42] prepared NCO@graphene quantum dots (NCO@GQDs) composite with tremella like structure where NCO is homogeneously encapsulated by GQDs using solvothermal method. In their synthesis route, GQDs were synthesized bottom-up approach first. These GQDs were added to precursor solution in the solvothermal method. The synergistic effect of both tremella like NCO and the conductive GQDs in the composite form exhibited good C_s of 1242 Fg^{-1} at 30 Ag^{-1} with 99% capacitance after 4000 cycles.[42] NCO/GQDs were synthesized by incorporation of GQDs in NCO host and used this composite as an electrode material for electrochemical energy devices. Interestingly, the synergistic double layer capacitive and pseudocapacitive characteristics from GQDs and NCO QDs provide a good C_s of 302 Fg^{-1} at a current density of 1 Ag^{-1}.[43] These two approaches are highly encouraging and motivated us to perform our comprehensive work on NCO/GQDs composites with variable concentration of GQDs. Our goal is to demonstrate the exceptional energy performance using the quantum dots integrated into a binary metal oxide material for supercapacitors. Our approach is based on fine tuning the chemical composition by performing extensive studies in a wide composition range. Therefore, in the present work, NCO/GQDs with different weight percentages (0–15%) have been prepared by hydrothermal method and studied their structural and electrochemical properties thoroughly. The particle size and morphology can be easily controlled by the simple hydrothermal method, which is well suited to synthesize high quality materials for application in electronics and energy technologies. Hydrothermal method has many advantages such as a large variety of forms can prepared with high quality, no need to use high temperature for reaction, low instrument cost, ecofriendly etc., Because of these reasons, in our work, an attempt has been made to synthesize pristine NCOQDs and NCO/GQDs using hydrothermal synthesis method. In addition to deeply studying their fundamental materials properties and phenomena, their performance metrics and application potential in both asymmetric and symmetric supercapacitors were evaluated.

2. Results and Discussion

2.1. Material Characterization

2.1.1. Crystal Structure, Phase, and Chemical Bonding

The crystallographic structure and phase-stabilization analyses of pristine NCOQDs and NCO/GQDs were made using detailed X-ray diffraction (XRD) studies. The XRD data of pristine NCOQDs and NCO/GQDs are shown in Figure 1b. The data shown is as function of variable amount of GQDs. The XRD patterns of all the samples exhibit the intense peak at $2\theta = 36.72°$ indicating the predominant (311) orientation. Along with (311) peak, the other characteristic XRD peaks identified are (111), (220), (222), (400), (511), and (440), which originated at 2θ values of 18.96°, 31.12°, 38.38°, 44.56°, 59.18°, and 64.92°, respectively. All these peaks are indexed to spinel structure of $NiCo_2O_4$ phase with $Fd\bar{3}m$, 227 space group (JCPDS Card No:73-1702). No other additional peaks were detected except the peak (002) at $2\theta = 26.4°$ (indexed with *), which corresponds to graphene. Thus, the XRD peaks and their assignment concludes that all the prepared samples are composites with successful graphene integration into NCO in addition to validating the fact that they are phase pure without any noticeable impurity.[44] Also, the appearance of common peaks and similar features in XRD patterns indicate that all NCO composites crystallize in the basic structure of $NiCo_2O_4$ spinel. The lattice parameter, which is calculated by least-square fitting using three Bragg lines, found to be $a = 8.10$ Å for pristine NCO, which is in good agreement with the literature. The low intensity of XRD patterns obtained for NCO-QD composites signifies the screening of NCO reflection by the presence of graphene.[45] These results evidenced that the graphene integrated into the composite or its variable concentration within the range considered in this work has no considerable impact on the crystal structure of NCO in the composites except the successful formation of NCO/GQD composites.

The crystallite size (D) of the samples is calculated using Debye-Scherrer's equation:

$$D = \frac{K\lambda}{\beta \mathrm{Cos}\theta} \quad (1)$$

where K is the Scherrer's constant, λ is the wavelength of x-ray radiation, β is the full width half maxima (FWHM) of a diffraction peak expressed in radian and is diffraction angle. For NCO/GQDs with variable GQDs content, the average crystallite size is calculated by considering the most intense (311), (400), and (511) reflections. The crystallite size thus determined was found to be 8.93, 5.83, 4.1, and 6.0 nm for pure NCO-QDs, NCO/GQDs-5%, NCO/GQDs-10% and NCO/GQDs-15%, respectively. The observed reduction in the crystallite size in the NCO composites implies that, in presence of carbonaceous materials, the crystallite growth is reduced during synthesis process.[46] Moreover, the absorbability and amorphous like layer of graphene slows-down the crystallite growth of NCO.[47] It can be observed that the XRD patterns of NCO composites display weak intensity and broad (FWHM) diffraction peaks over NCO-QDs because of the fact, when the crystallite size decreased, and broadening of the diffraction peaks was a consequent reaction.[48] The small increment in the crystallite size at NCO/GQD-15% may be due to higher concentration of graphene inculcation. The reduction in the peak intensity of NCOQD nanocomposites signifies that the crystalline materials with lower size could provide higher number of electroactive sites for penetration and diffusion of ions. This could enhance the performance of the capacitive behavior.

To further confirm the structural features, phase formation of NCO/GQDs, and probe the chemical bonding

information, we relied on Raman spectroscopic characterization of the NCO/GQD samples. The structure, phase, and chemical bonding of simple and complex materials at all length scales can be probed effectively using Raman spectroscopy, which is a simple yet versatile nondestructive technique.[49–51] The Raman spectra recorded for pristine NCOQDs and NCO/GQDs are shown in Figure 1c. Raman spectra recorded in the broad frequency range of 100–2000 cm^{-1} reveal important information on the characteristic chemical bonds present in the samples. It is evident that the NCOQDs and NCO/GQD-composites contributed to the spectral features, which represents the combination of both NCO and carbon, particularly those in the low wavenumber (100–1000 cm^{-1}) and high wavenumber (1200–2000 cm^{-1}) regions. The pristine NCOQDs spectrum exhibits five apparent Raman peaks at 183, 472, 520, and 655 cm^{-1}, which are attributed to F_{2g}, E_g, F_{2g}, and A_{1g}, respectively, vibrational modes of spinel cubic NCO. The strong Raman vibrational modes obtained in the region of 500–700 cm^{-1} can be attributed to stretching vibrations of oxygen atoms in the octahedral unit.[52] The E_g mode is attributed to the asymmetric bending mode of O—Co—O that is, the vibration of oxygen atom in ab-plane, while the A_{1g} mode is assigned to the symmetric stretching mode of Co—O that is, the vibration of oxygen atoms along the c-axis.[53]

The Raman spectral features of carbon can be observed at wavenumbers 1350 and 1575 cm^{-1}, 1361 and 1579 cm^{-1}, 1389 and 1587 cm^{-1}, respectively, as disorder D-band and graphitic G-band for NCO/GQD with variable GQD content. The D-band is called as "disorder induced band" that originates due to vibration of carbon lattice disturbed by edges or defects (K-point phonons with breathing mode of A_{1g} symmetry). Whereas graphite G-band is the contribution of primary in-plane breathing mode of hexagonal sp^2-carbon rings in graphite (E_{2g} phonons).[54,55] The slight broadening nature of Raman bands in the range of 300–700 cm^{-1} for NCO/GQDs composites signifies the interaction of carbon with metal oxides. A broad and low intensity peak observed at 1069 cm^{-1} can be assigned to D″-band of carbonaceous traces in the composites. D″-band corresponds to a combination of D phonon and a phonon related to the longitudinal acoustic (LA) mode.[9] The amount of disorder causes increment/decrement of intensity of D-band. The ratio of peak intensities I_D/I_G generally indicates the degree of graphitization in the NCO/GQDs composites.[56] The NCO/GQD-5%, NCO/GQD-10%, and NCO/GQD-15% nanocomposites, that is, NCO with variable graphene, exhibit I_D/I_G values of ≈0.84, 0.86, and 0.87, respectively. These I_D/I_G values indicate the graphitization degree of NCO/GQDs-10% and NCO/GQDs-15% is comparatively higher. The high graphitization degree in the composites results in improving the electrical conductivity and specific capacitance as seen under electrochemical studies discussed subsequently.

2.1.2. Morphology and Microstructure

The morphology and microstructure characteristics of the NCO/GQD nanocomposites were examined by means of electron microscopy analyses. The scanning electron microscopy (SEM) data of NCO/GQD nanocomposites are shown in **Figure 2**, where the surface morphological features of the samples as a function of GQD content are evident. The high (100 nm; Figure 2a) and low (300 nm; Figure 2b) magnification SEM images illustrate the homogeneous distribution of the particles with an average size of 5–10 nm range. This characteristic feature infers the quantum dots formation successfully occurred using hydrothermal synthesis. Figure 2c–h displays the well-distributed nanoscale particles in all the NCO/GQD composites. The introduction of GQDs into NCO results in evenly distributed particles with comparatively less in size over pristine NCOQDs. Moreover, the interconnecting nature of the particles can be observed clearly in NCO/GQDs composites. No significant changes in the morphology of NCOQD after graphitization elucidates graphene successfully coated on the surface of NCO particles. Also, substantial improvement in the binding and conducting agents favors the formation NCO/GQDs composite. In the hydrothermal route, the electrostatic, dipole-dipole interactions and representatives of hydrogen bonding have been determined because functional groups exist on the surface. These functional groups help in the formation of graphene quantum dots and interacting with Ni (II) and Co (III) cations in addition to urea.[53] This reaction mechanism is responsible for the crystal growth and tuning the morphology for NCO composites. The strong interactions of residual oxygen functional group of GQDs contains oxygen residual or van der Waals of GQDs with NCO structure that can be observed in the NCO/GQDs composites.[57] The NCOQDs are evenly dispersed and extended in all directions. On the other hand, NCO and GQDs are interconnected, well-connected graphene adheres closely on the surface of the NCOQDs to enable a conductive network. This conductive network facilitates a robust anchoring between NCO particles and provoke fast electronic transport resulting in remarkable improvement in the cycle stability of the composites.[43] Figure 2g,h displays the quantum dots with agglomeration for NCO/GQDs-15% sample. The high concentration of (15%) GQDs made the larger particles due to agglomeration. Too much carbon coating is also not good, it won't allow clear particles formation. If a dense carbon coating layer is applied as an external support to binary transition metal oxides, not all these carbonaceous materials may positively contribute to the electrochemical properties.[58] They often render the energy of ions/electrons into metal oxides. Besides, the overuse of GQDs may reduce the capacitance owing to lower capacity of carbon. Therefore, based on the structure, phase, surface morphology, chemical bonding analyses made, NCO/GQDs-10% appears to be the better candidate and optimum composition to derive enhanced supercapacitor performance. The energy dispersive spectrometry (EDS) data demonstrated Ni, Co, O, and C elements with their corresponding binding energies for all the samples (Figure S1 and Table S1, Supporting Information). Thus, the chemical homogeneity of the NCO/GQDs is evidenced in EDS analyses in addition to X-ray photoelectron spectroscopic analyses discussed subsequently.

The average grain size is estimated from the standard analytical technique of particle size distribution (PSD) obtained from analysis of scanning electron microscopy (SEM) images. The data obtained for intrinsic and NCO QDs and NCO/GQDs are shown in Figure S2a–d (Supporting Information). The estimated grain size for all the four samples from the PSD are in the range of 4–10 nm respectively, that confirms the formation of QDs. The average particle size obtained from PSD decreases from 10 to

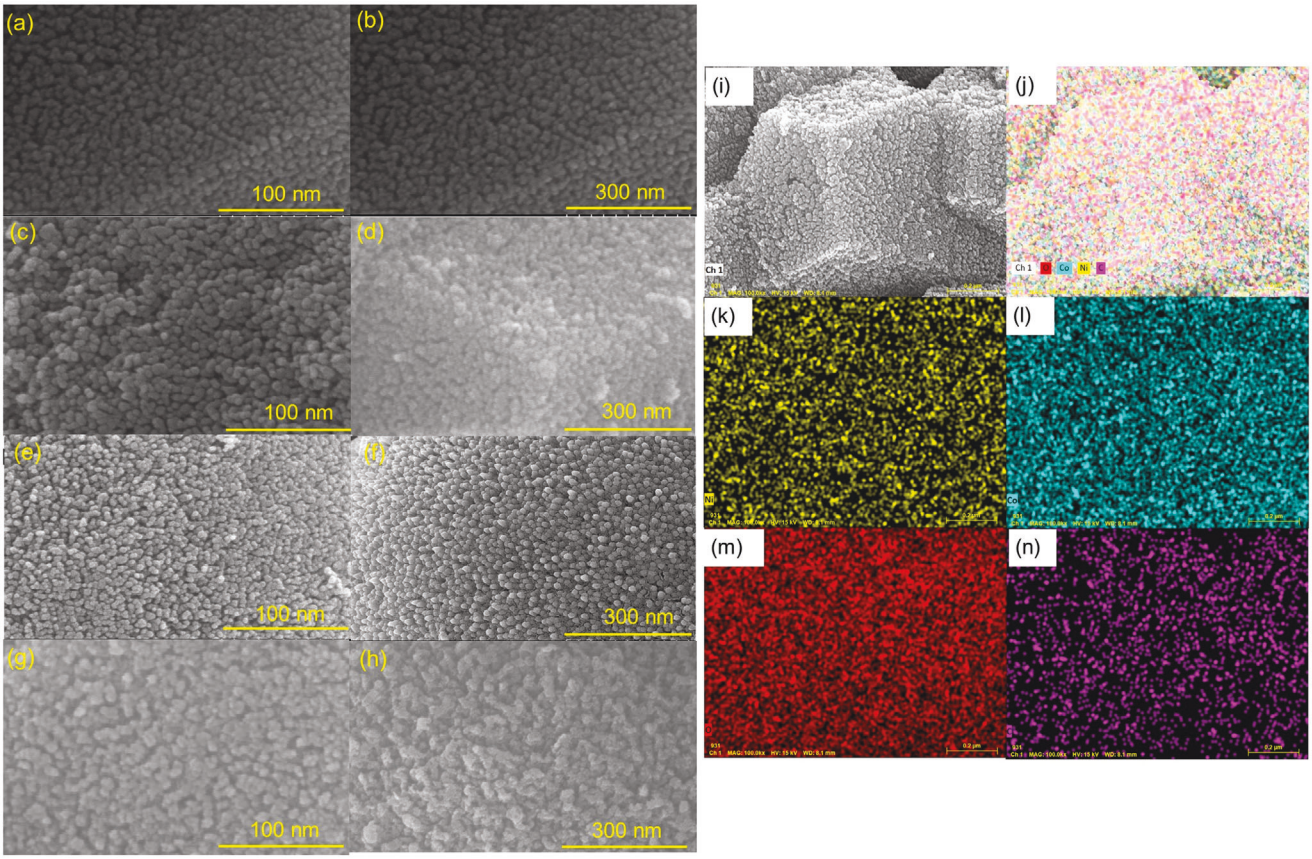

Figure 2. SEM data of NCO/GQDs as function of GQDs content. SEM images shown with high (100 nm) and low (300 nm) magnification for: pristine NCO/QDs (a,b), NCO/GQDs-5% (c,d), NCO/GQDs-10% (e,f), NCO/GQDs-15% (g,h); Elemental mapping of NCO/GQDs-10% from SEM analysis (i) for all elements [Ni, Co, O, C] (j), Ni element- yellow color (k), Co element – green color (l), O element-red color (m), C element – pink color (n), respectively.

4 nm after graphtization in the order $L_{NCOQDs} > L_{NCO/GQDs\text{-}5\%} > L_{NCO/GQDs\text{-}15\%} > L_{NCO/GQDs\text{-}10\%}$. The NCO/GQDs-10% sample has the narrower PSD compared with others. It is attributed to the effect of respective graphitization, which can retard the crystallite size of the particles. This tendency was also observed in the XRD studies. It can be noted that both analyses (XRD and FE SEM) demonstrate that the quantum dot size (L_c < 10 nm) was easily obtained via hydrothermal route. Among all the samples, GQDs-10% in NCO framework make a clear particle with fine tuning of 5 nm respectively. This least particle size not only provides high electrical conductivity but also facilitates excellent surface area, which leads to improvement in the electrochemical performance of the composites.

The microstructure, morphology, and crystallographic characteristics of NCO/GQD nanocomposites were further investigated by high-resolution transmission electron microscopy (HR TEM). The low-magnification TEM images, selected area electron diffraction (SAED) patterns, and HR-TEM images of NCO/GQDs as a function of varying GQD amount are shown in **Figure** 3a–p. The high and low magnification bright field TEM images (Figure 3a,b) of pristine NCOQDs indicate uniform dispersion of nanoscale spherical-shaped particles. These particles are well separated from each other and possess an average particle size of 10 nm, which is consistent with XRD data. Combined with the results of all other structural and chemical bonding characterizations, the TEM results also imply that the formation of quantum dots occurred successfully. Figure 3e,f,i,j,m,n shows the TEM micrographs of NCO/GQDs-5%, NCO/GQDs-10%, and NCO/GQDs-15% composites. In all these composites, graphene sheets are well dispersed and connected to quantum dots of NCO particles then manifest a conducting network with a strong connected architecture.[59] It can be observed that different percentage/amount of graphene coating on NCO does not alter the particle morphology. However, the reduced particle size can be observed and the estimated particle size for all the three samples decreases from 9 to 5 nm, in the order of $L_{(NCO/G\text{-}5\%)} > L_{(NCO/G\text{-}15\%)} > L_{(NCO/G\text{-}10\%)}$. Whereas the agglomerated particles can be observed for $L_{(NCO/G\text{-}15\%)}$ with slightly increased particle size. The NCOQDs are evenly dispersed among the graphene and extended in all directions like a stretched network and the well-connected graphene adhere closely on the surface of the NCO-QDs that make a conductive network.[60] This conductive network facilitates a robust anchoring between NCO particles and provoke fast electronic transport resulting remarkable improvement in the cycle stability of the composites.[61,62] It can be noticed that Figure 3m,n displays some of the agglomeration for NCO/GQDs-15% sample due to high content of carbon. The data corroborates with SEM analyses.

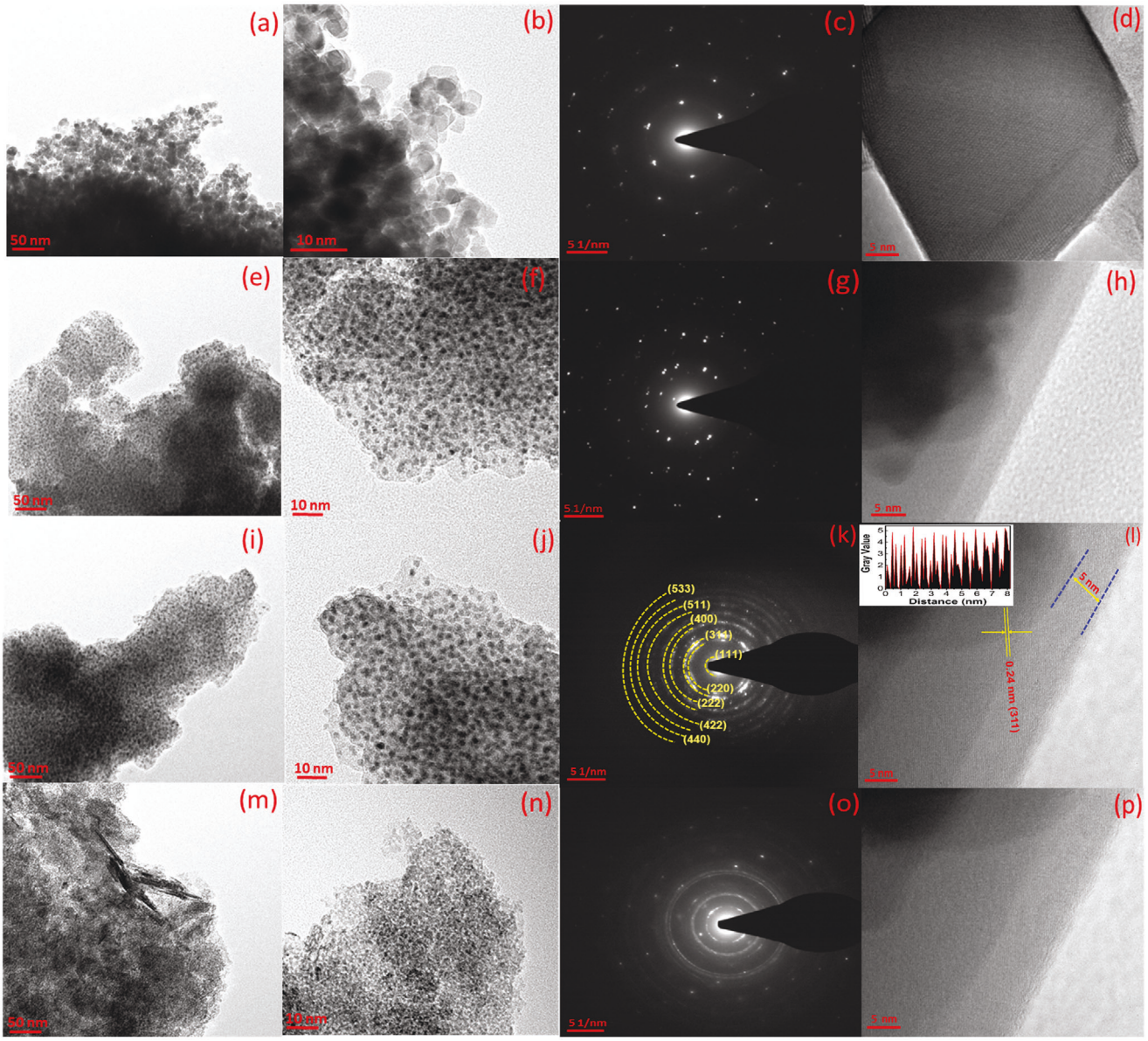

Figure 3. TEM images with low (50 nm) and high magnification (10 nm), SAED pattern and HR TEM image of pristine NCO/QDs (a–d), NCO/GQDs-5% (e–h), NCO/GQDs-10% (i–l), and NCO/GQDs-15% (m–p). The HRTEM mages clearly show the crystalline nature with presence of fringes with the inter-planar spacing of 0.247 nm for NCO (311) and 0.21 (002) for Graphene, respectively, corresponding to the NCO/GQDs spinel structure.

Figure 3c shows SAED pattern of NCOQDs sample that clearly shows bright spots infers that the NCOQDs obtained are crystalline in nature,[63] which is consistent with the XRD data. The SAED patterns (Figure 3g,k,o) of NCO/GQDs (5%, 10%, and 15%) composites elucidate partial bright spotted diffused diffraction rings for all the three samples signifying the surface of the NCOQDs coated with thin graphene layer. Among all the samples, NCO/GQDs-10% (Figure 3k) demonstrates clear diffraction rings corresponding to diffraction from (111), (311), and (221) planes indicating that this composite formed very similar to the pristine NCO. This observation also corroborates with XRD analysis. The HRTEM images of all the samples are shown in Figure 3d,h,i,p. All the samples manifest well-resolved lattice fringes with an interplanar distance of 0.24 nm corresponding to the *d*-spacing of (311) planes of cubic NCO. Figure 3h,l,p shows another lattice spacing value of 0.21 nm, which belongs to graphene in addition to 0.24 nm (311) plane. This corresponds to diffraction from (002) plane of GQDs that confirms the formation of NCO-GQDs composites.[64] These graphenization surfaces not only connect the NCOQDs with GQDs but also stick as a thin pseudo coating of 1–2 nm on NCO structure that retard the crystal growth and reduces the crystallite size. The graphene coating with 2 nm favors their high pseudocapacitive performance.[65] In presence of inorganic substance, carbon can retard the crystal growth of binary transition metal oxide. The greater absorbability and amorphous nature of carbon easily controls the particle

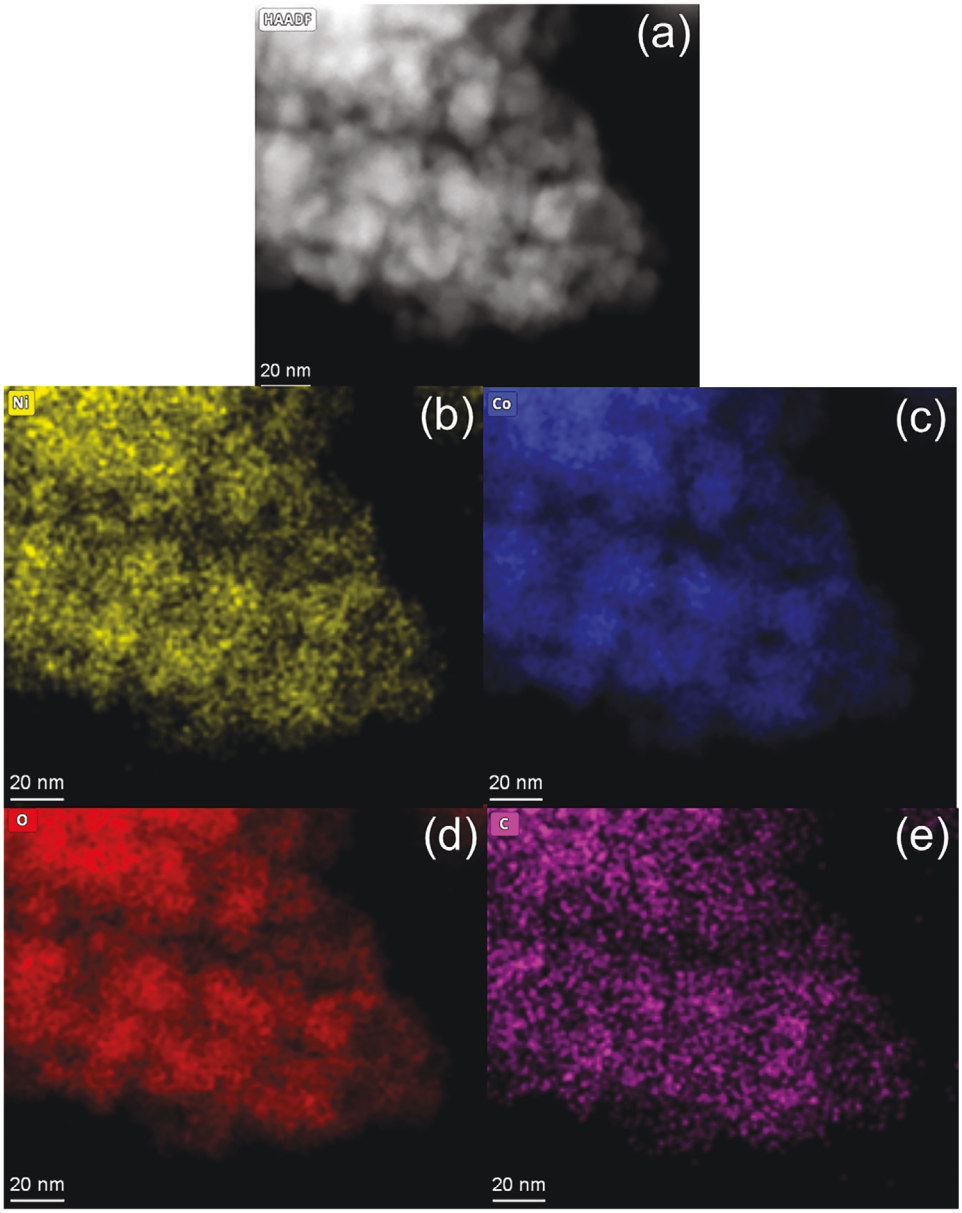

Figure 4. Elemental mapping of NCO/GQDs-10% from TEM analysis. HAADF image of NCO/GQDs-10% (a), Ni element-yellow color (b), Co element-blue color (c), O element-red color (d), and C element-pink color (e), respectively.

size. The estimated average crystallite sizes are in the range of 10–4 nm. The quantum dots will have enormous surface to volume ratio and facilitate the mechanical strength that avoids the peeling of the material during charging–discharging leading to high capacitance to the electrodes. Elemental mapping characterization was conducted on the selected composition (NCO/GQDs-10% composite). The data shows different elements exist in the composite. In **Figure** 4a–e, the data shown are: HAADF images of NCO/GQDs-10% (a), Nickel-yellow (b), Cobalt -blue (c), Oxygen-red (d), and Carbon-pink (e). Similar to elemental mapping of SEM Figure 2i–n, the HAADF imaging analysis also indicates the chemical homogeneity and uniform distribution of all the elements in the NCO/GQDs.

2.1.3. Thermal and Chemical Stability

Thermogravimetric analysis (TGA) experiments were performed on pristine NCOQDs and NCO/GQDs-10% composites. The data obtained are shown in Figure S3a,b (Supporting Information). TGA carried out in the temperature range of 25–800 °C allowed us to understand and verify the thermal stability of the synthesized samples. From the TGA graphs, in the range of 200–400 °C, a weight loss of 3.85% and 2.79% can be noted for NCOQDs and NCO/GQDs-10% composites, respectively. These weight losses can be explained as follows. i) TGA curves indicate gradual weight loss of 1.5–2.0% between RT-200 °C that is attributed to the evaporation of physically adsorbed water molecules.[66] ii) In

the second step, small weight loss ≈1.5% can be observed for both pristine and GQDs integrated samples which accounts for removal of water formed by the de-hydroxylation of hydroxide layer.[67] After the second step, no apparent weight loss occurs. This observation indicates that the material/composite displays a behavior of a single unit for further raise in the temperature. This data confirms the formation of NCOQDs from its precursors starts between 350 and 400 °C. In the NCO/GQDs-10% sample, thermal decomposition of oxygen containing functional groups is noted. The NCO/GQDs-10% composite has shown apparent least weight loss of 2.79% (weak exothermic peak) at 350–400 °C comparing to the pristine NCOQDs (3.85%) ascribed to burning of graphene flakes into fragments. It confirms the exothermic reaction happening in NCO/GQDs-10% composite. The observed weight loss is rather low for both intrinsic and graphene-integrated composite samples signifying that, both the NCOQDs and NCO/GQDs-10% composites are thermally stable not only because of presence of Ni and Co metal moieties but also quantum dot nature. Additionally, it should be highlighted that neither NCOQDs nor their composites present any clear weight loss at high temperatures. This observation suggests that the hydrothermal process is highly beneficial to create thermally stable NCOQDs and NCO/GQD composites. Overall, these TGA results reveal that the optimum calcination temperature of NCOQDs and NCO/GQD-composites is ≈400 °C, which corroborates with the reports exist in the literature.

2.2. Surface Chemistry, Physical Characteristics & Porosity, and Chemical Valence States

2.2.1. Chemical Composition and Chemical Valence States–XPS

X-ray photoelectron spectroscopic (XPS) studies allowed us to derive further insights into surface chemistry, elemental/chemical composition, electronic structure, and chemical valance states of intrinsic NCO/GQDs nanocomposites with variable composition. **Figure** 5a shows the XPS data of intrinsic NCOQDs and NCO/GQDs nanocomposites. The survey spectra are shown in Figure 5a, where the observed XPS peaks are primarily due to Ni 2p, Co 2p, and O 1s peaks along with C 1s. These peaks and their corresponding binding energies (BE) are as indicated in Figure 5a. The unit cell and graphene coated unit cell of $NiCo_2O_4$ are shown in Figure 5b-i,ii. The core-level XPS spectra of Ni and Co metal cations is of particular interest to understand the effect of processing as well as graphene integration. High resolution XPS spectra obtained from Ni 2p, Co 2p, O 1s, and C 1s are shown in Figure 5c–f respectively. The spectrum of Ni 2p, Co 2p, O 1s, and C 1s are fitted with Shirley background in their respective BE values and followed by Lorentz-Gaussian (LG) fitting.[68] Only the core-level XPS spectrum of Ni $2p_{3/2}$ region is shown in **Figure** 6c for simplicity. Most of the transition metals show multiplet splitting due to the coupling between un-pair electrons in the core levels and outer shells.[69–77] Following the procedure developed by Biesinger, we are also deconvoluted the Ni $2p_{3/2}$ peak with several multiplet peaks with a linear combination of Ni^{2+} states and Ni^{3+} states.[71,78]

All the peaks from the Ni^{2+} state are shown in blue color while the Ni^{3+} state are shown in pink color. The high-resolution Ni $2p_{3/2}$ spectra of pristine NCOQDs and NCO/GQDs (5%, 10%, and 15%) composites are shown as individual spectra with clear Ni^{2+} and Ni^{3+} oxidation peaks for better understanding and are given as Figure S4 (Supporting Information). Different oxidation state values of Ni^{2+} and Ni^{3+} of Ni $2p_{3/2}$, FWHM, peak position, and % concentration values of NCOQDs and NCO-GQDs (5%,10%, and 15%) composites are shown in Table S6 (Supporting Information). The XPS spectra peak fitting is similar to all the samples and is shown in Table S2 (Supporting Information). From these fittings, it is clear that pure NCOQD and its composites contain a mixture of Ni^{2+} and Ni^{3+} in tetrahedral environment.[78] However, pure NCOQD exhibits a higher concentration of Ni^{2+} compared to Ni^{3+}. On the other hand, the integration of GQDs into the NCO frame leads to a reduction in the proportion of Ni^{2+} and increase the presence of Ni^{3+} states. The oxidation portion ratios values of Ni^{2+} and Ni^{3+} in Ni $2p_{3/2}$ for all the four samples are given in **Table 1**. Figure 5d displays high resolution core-level spectrum of Co $2p_{3/2}$ region between the BE values of 777–792 eV. Like Ni, Co 2p also shows multiplet peaks. As such, we applied a similar fitting approach as we did for Ni by combining 2+ and 3+ states. We took a similar approach like Ni and fitted the Co $2p_{3/2}$ with the combination of 2+ and 3+ states similar to the one observed in the Co_3O_4 phase.[78] The fitted Co 2p values of all the four samples are shown in Table S3 (Supporting Information). These results suggest that NCOQDs frame mainly consists of mixture of Co^{2+}/Co^{3+} in an octahedral and tetrahedral environment.[79]

The core level XPS peaks of O 1s are shown in Figure 5e. The O 1s exhibits four oxygen components. The first component originated at BE of 529.67 eV, which is attributed to the formation of oxides with metal (either Ni or Co), that is, metal-oxygen bond corresponding to lattice oxygen. The second component, located at a BE of 531.27 eV is associated with oxygen in hydroxyl (OH—) functional groups. The presence of this component confirms that the NCOQDs sample is partly dehydroxylated and corroborates to the synthesized compound in nanoscale that formed with defect sites along with low oxygen co-ordination at the surface.[80] The third component originated at 532.20 eV is ascribed to the oxygen bond with the carbon (C—O). The final O 1s component located at BE value of 533.67 eV corresponding to the C═O bond originated due to single ketones decorated on the edges of graphene sheets. This C═O is also possible to bound to the basal plane as carbonyl groups within the surface of NCO. The high-resolution spectra of C 1s reflects six characteristic peaks at BE value (for pure NCOQDs sample) at 284.20, 285.05, 286.70, 288.20, 289.20, and 291.11 eV. The first two peaks in the lower binding energy sides are attributed to C═C sp^2 bond at 284.20 eV and C-C sp^3 at 285.05 eV, respectively.[81] The XPS peak located at BE value of 286.70 eV is ascribed to hydroxyl group, in which carbon is bonded with either (hydroxyl ion) C═OH or C—O—C. The remaining two peaks located at BE values of 288.20 (C═O) and 289.20 eV (O—C═O) were corresponding to carboxylic functional group. The C═O bonds originated due to single ketones decorated on the edges of graphene sheets. This C═O is also possible to bound to the basal plane as carbonyl groups.[82] Another carboxyl peak is formed due to the bonding with oxygen. The satellite peak at the tail of the spectrum with high BE value originated at 291.11 eV corresponding to π–π interaction. It can be noted that, in the NCO/GQDs nanocomposites with a variable

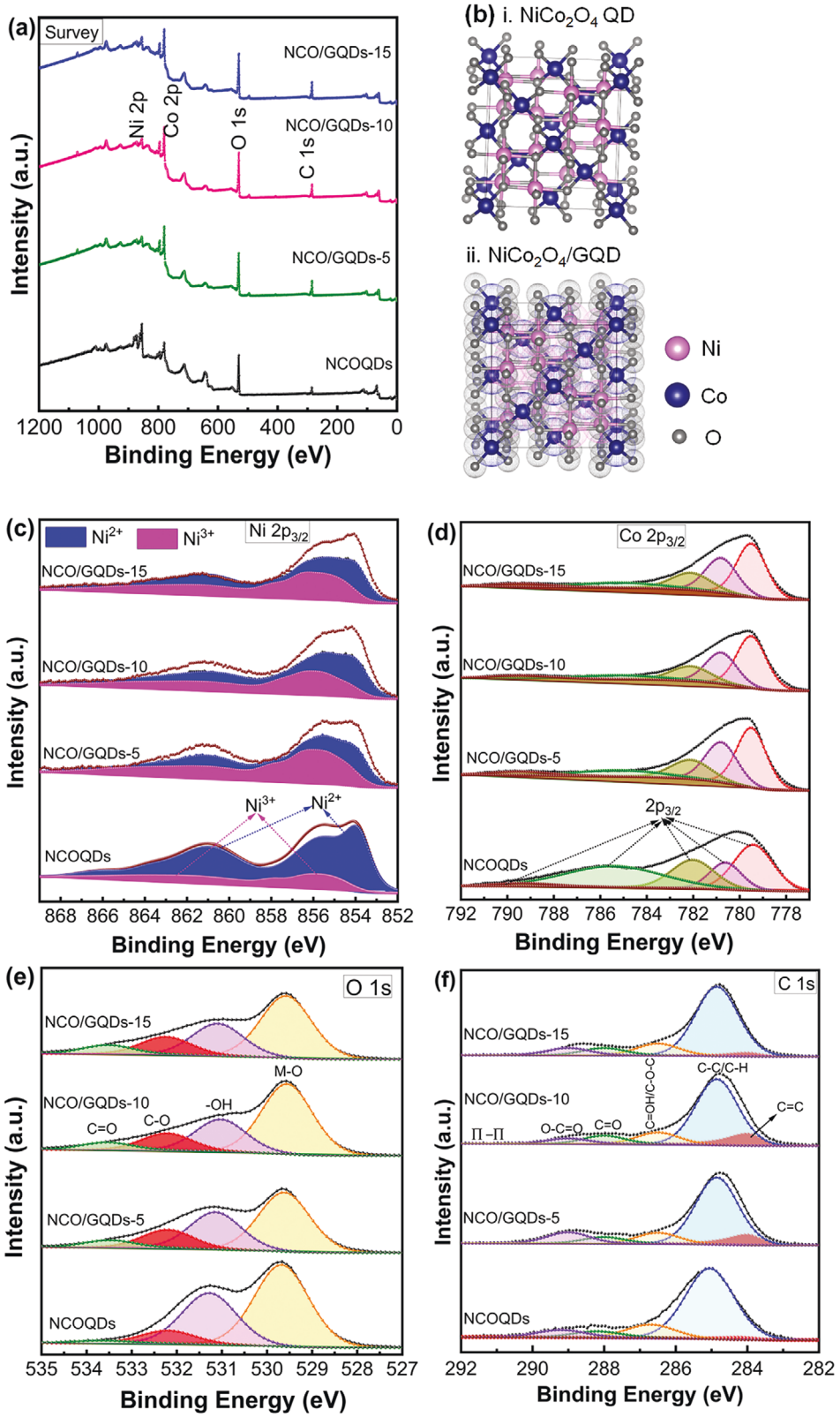

Figure 5. a) XPS survey spectra data of NCOGQDs composites with variable GQD content. XPS analyses of intrinsic NCOQDs are also presented for comparison. b) The unit cell (i) and graphene coated unit cell (ii) of $NiCo_2O_4$. The data shown are the high-resolution spectra of c) Ni $2p_{3/2}$; d) Co $2p_{3/2}$; e) O 1s; f) C 1s, respectively.

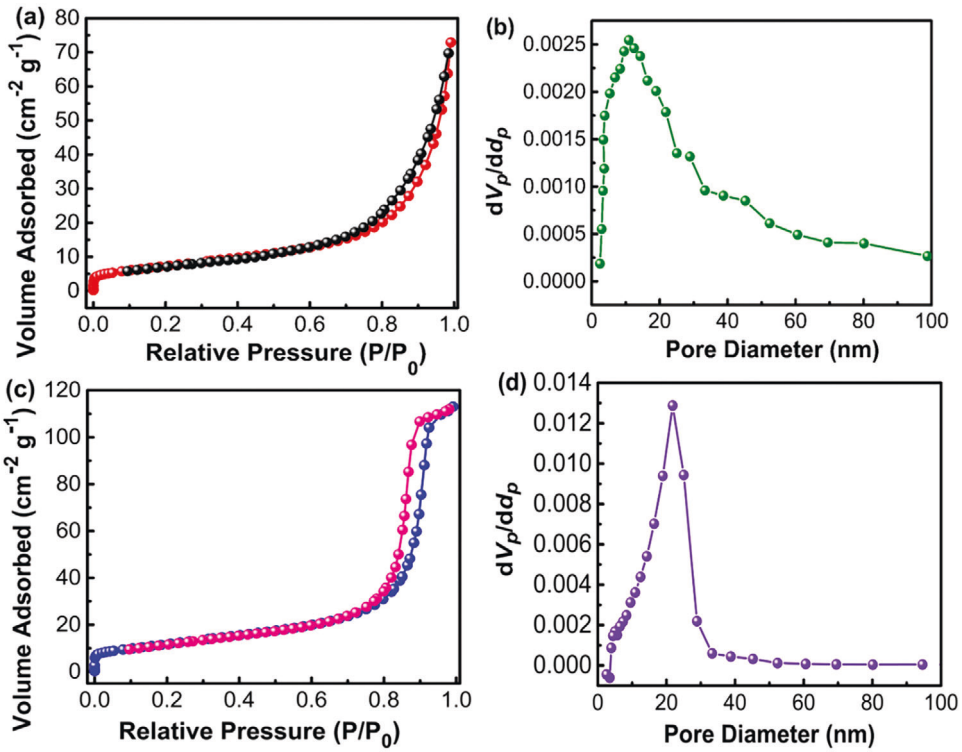

Figure 6. Nitrogen adsorption–desorption isotherms and the corresponding DFT pore size distribution of pristine NCOQDs (a) and, NCO/GQDs-10% sample (b), respectively.

graphene content, the Ni and Co characteristics peaks are almost in the similar range of BE values of pure NCOQDs whereas O and C have shown some deviation due to graphitization during the synthesis process. The respective binding energy values (O 1s and C 1s) are presented in Tables S4 and S5 (Supporting Information). The XPS data, particularly the core-level XPS data of Ni, Co, and O, indicate that the addition of graphene does not change the chemical structure. The atomic weight percentage values of C, Co, Ni, and O elements obtained from XPS survey spectra for the four samples are given in **Table 2**. It can be noticed that the carbon atomic wt% is only 12.91% in pure NCO whereas 13–14% in the NCO/GQDs composites infer that the graphene integration has successfully occurred using hydrothermal method. The introduction of GQDs into NCO framework causes to form NCO/GQDs composites. This functional carbon formation a strong bonding of C-O-Ni/Co between GQDs and spinel NCOQDs. Moreover, GQDs act as electron donors, which help transformation of charge from GQDs to NCOQDs.

Table 1. Oxidation portion ratio values of Ni^{2+} and Ni^{3+} in the Ni $2p_{3/2}$ for all the four samples are given below.

Sample Code	Ni^{2+}	Ni^{3+}	Ni^{3+}/Ni^{2+}
Pure NCO	87	13	0.2
NCO/GQD-5	40	60	1.5
NCO/GQD-10	56	44	0.8
NCO/GQD-15	48	52	1.1

The successful coating of GQDs on NCOQDs samples caused NCO-GQDs composites those maintained graphitic sp^2 structure much favoring the electrical conductivity.[83]

2.2.2. Surface Physical Characteristics and Porosity

The specific surface area, pore size distribution, and pore volume of the synthesized NCOQDs and NCO/GQDs-10% nanocomposites are further characterized by N_2 adsorption/desorption isotherm and shown in Figure 6a–d. A Langmuir type IV isotherm has been noticed with a hysteresis loop in the relative pressure range of 0.8–1.0 for the two samples (in Figure 6a–d, signifies the two samples exhibit mesoporous nature (2–50 nm). It can be noticed that the sharp increase in the adsorption at small relative pressure indicating the existence of mesoporous nature.[48] This mesoporosity can provide the faster diffusion of charge species (electrons and ions) to the NCOQDs electrodes. There are distinct hysteresis loops observed in the hysteresis loop range from 0.7 to 1.0 P/P_o. The BET specific surface area of the synthesized NCOQDs and NCO/GQDs-10% samples (Figure 6b,d) found to be 26.43, and 42.27 $m^2\ g^{-1}$, respectively. The Barret–Joyner–Halenda (BJH) method was used to calculate the pore size distribution and pore volume using desorption isotherm of two samples.

The NCOQDs and NCO/GQDs-10% samples show average pore size of 8.25 and 8.04 nm, respectively, and the pore volume of 0.115, and 0.174 $cm^3\ g^{-1}$, respectively. The results suggest that the NCO/GQD composites have a large surface and least

Table 2. Chemical composition (atomic wt%) of different elements in the NCOQD and NCO/GQD samples obtained from the XPS survey spectra are given below.

Sample Code	Ni	Co	O	C
Pure NCOQD	19.68	39.37	28.05	12.91
NCO/GQD-5	19.35	39.01	28.59	13.06
NCO/GQD-10	19.27	38.27	29.27	13.25
NCO/GQD-15	21.05	39.10	25.10	14.76

pore size over NCOQDs, indicating that well-dispersed graphene sheets adhere closely on the surface of the NCO particles, which form conductive architecture that helps to accelerate the fast electron transport.

The high surface area and conductive network of NCO/GQDs-10% composites can increase the effective contact area between the electrode and electrolyte interfaces that facilitate large number of electroactive sites for the electrochemical reactions during charge–discharge process. Particularly, the low porosity and high pore volume could help to transport and diffusion of the electrolyte ions during rapid charging-discharging at high current rates. Moreover, the porosity avoids the stress and prevents the volume change that caused by ions during charge–discharge process resulting in the improvement in the cycling stability.[79] The large volume of the samples not only provides reservoirs for ions but also improves the diffusion kinetics. The narrow and orderly distributed pores with size ≈8.04 nm of the NCO/GQDs-10% sample enhances the electrochemical process; these pores can facilitate more facile penetration of electrolyte within the pores for rigorous faradaic redox reactions and double layer charge–discharge process.

2.3. Electrochemical Properties and Performance Evaluation

2.3.1. Cyclic Voltammetry

The electrochemical behavior of the NCO/GQD nanocomposites was evaluated employing a three–electrode aqueous cell, the NCOQDs and NCO/GQDs composites were used as the working electrodes. A platinum metal strip and Ag/AgCl were used as counter and reference electrodes in the presence of 1 mole saturated Li_2SO_4 aqueous electrolyte. The electrochemical data are shown in **Figure** 7a–l. All the tests were conducted at room temperature (25 °C). Figure 7a,d,g,j) present the cyclic voltammetry (CV) curves of the NCO/GQDs nanocomposites in the voltage range of 0.0–0.6 V. The Li_2SO_4 aqueous solution was employed as electrolyte due to its high lithium concentration that possesses high ionic conductivity and reduces the electrode/electrolyte interfacial resistance. Moreover, it is non-corrosive, eco-friendly, cost effective, electrochemically stable, and facilitates a wide voltage range.[80] The CV curves of the NCO/GQD electrodes at different scan rates (1–300 mV s^{-1}) within the potential window of 0.0–0.6 V versus Ag/AgCl are shown in Figure 7a,d,g,j. The shape of these CV curves for all these electrodes transforms from a rectangular shape to quasi-rectangular shape without contributing obvious redox peaks. This observation implies a capacitive behavior of the electrodes governed by pseudocapacitance with non-faradaic contributions from the electrical double layer effect. The absence of obvious redox peaks in CV profile for all the electrodes indicate that the oxidation-reduction process of the electrodes-maintained pseudo constant rate.[58] As suggested by Wang et. al., when the particle size reduces to nanoscale dimensions, both capacitive (pseudocapacitive) and electrical double layer capacitance process could substantially occur because of high surface to volume ratio.[81] The integral area and current density of CV profile increases with increasing scan rate from 1 to 300 mV s^{-1} but the shape remains the same even at high scan rates ensures good reversibility and high kinetics at high rates during charge–discharge process. The CV profile of NCO composites displays quasi-rectangular shape with high currents ascribed to the strong interaction between NCO and residual oxygen containing functional groups on the GQDs or van der Waals interactions between NCOQDs and GQDs. At higher scan rates the rate of diffusion is more than the rate of reaction. Hence, more electrolytic ions reach the electrode electrolyte interface whereas very few ions participate in the charge transfer reaction. On the other hand, at higher scan rates, the electrolyte ions do not have sufficient time to oxidation/reduction process in addition to quick adsorption/desorption process near the electrode/electrolyte interface in the NCO matrix. At very high scan rates (between) 300–800 mV s^{-1}, the shape of the CV curves will be the same. The integral area and current density are observed to be increased. The quasi-rectangular nature of CV curves has improved to some extent. Thereafter, >800 mV s^{-1} we can observe more quasi-rectangular shape CV with reduced integral area. At the scan rate of 1 V s^{-1}, the CV curve can be completely turned to quasi-rectangular shape with the least integral area, but the current is observed to be same/constant. The more electrolytic ions reach the electrode electrolyte interface whereas very few ions participate in the charge transfer reaction. As per obtained data (we don't show here) that, at 1 V s^{-1} scan rate the CV curves remain constant there will be no improvement in the integral area and current density. The electrochemical reversibility storage mechanism of NCO can be elucidated in the following equations.[15]

$$NiCo_2O_4 + OH^- + H_2O \leftrightarrow NiOOH + 2CoOOH + 2e^{-1} \quad (2)$$

$$CoOOH + OH^- \rightarrow Co_2 + H_2O + e^- \quad (3)$$

Increasing the scan rate causes adsorption/desorption to occur in addition to oxidation/reduction at the surface of the bulk of electrode. The charge-storage is almost dominated by semi-infinite diffusion that may be due to some parts of the electrode having mixed meso- and nano-pores that are easy to access the entire surface. Similar tendency was noted for Li_2TiO_3, TiO_2, LaB_6, and Nb_2O_5 consistent with nanocubiod NCO particles prepared by hydrothermal method.[82] At lower scan rate, the oxidation/reduction of Li^+ occurs throughout the NCO crystal structure along with adsorption/desorption at surface of the entire electrode causing high capacitance. Hence the charge storage of NCOQDs samples can be expressed as a combination of both pseudocapacitive and electric double layer capacitance for all the scan rates (1–300 mVs^{-1}) in the potential cutoff of 0.0–0.6 V versus Li/Li^+. They are governed to determine the relative charge contributions from diffusion-controlled reaction and surface

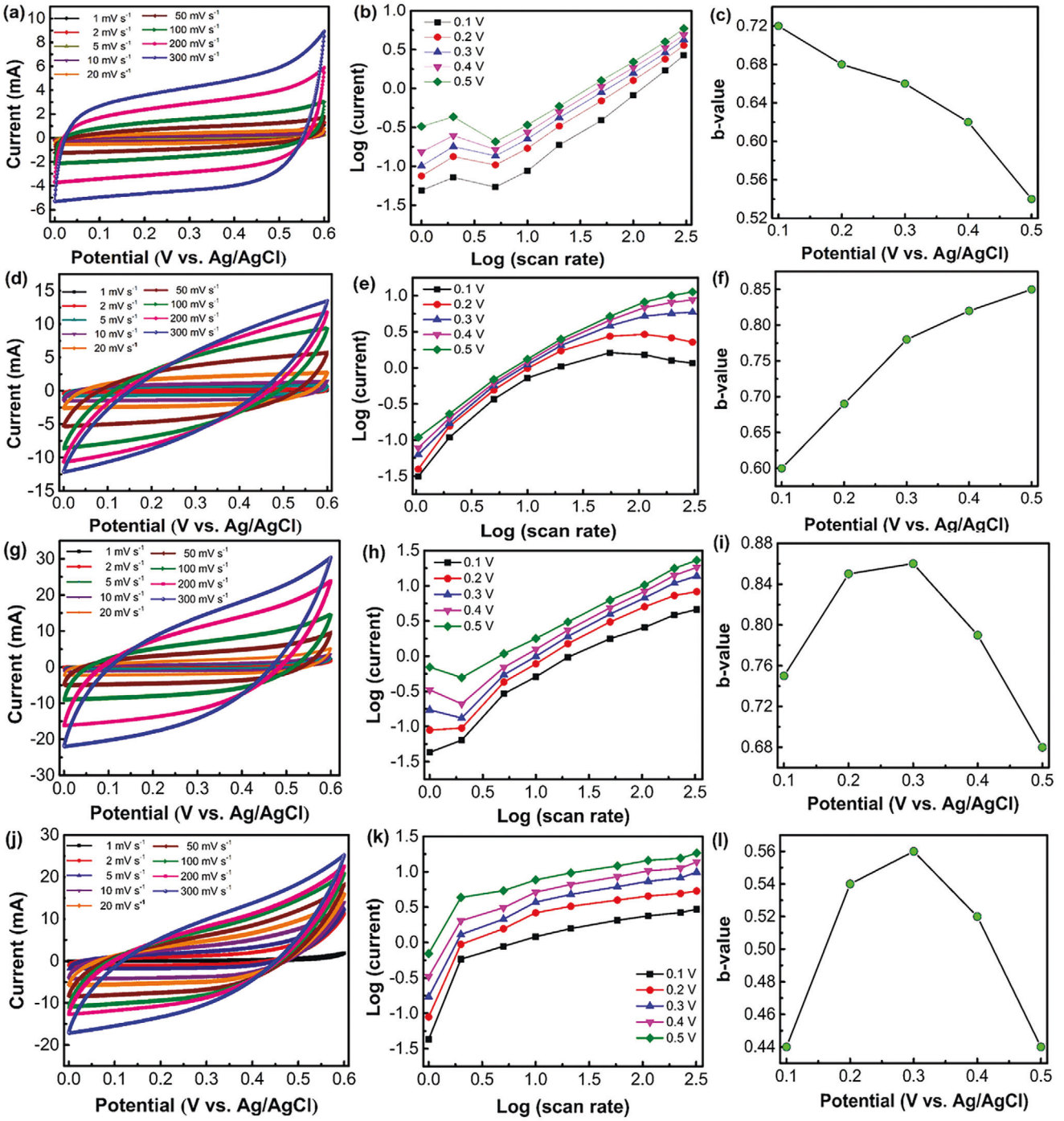

Figure 7. Voltammetric response of at different scan rates, variation of log(i) versus log (scan rate) for Power's law, and b-value plotted as a function of different potentials of NCOQDs (a–c) NCO/GQDs-5% (d–f), NCO/GQDs-10% (g–i), NCO/GQDs-15% (j–l), respectively.

effects. To confirm the electrochemical mechanism, we employed the standard power law (4):

$$I = Kv^b \tag{4}$$

where "I" is the current and "K" and "b" are the coefficients and "v" is the potential scan rate. The coefficient "b" takes values from 0.5 to 1.0; the magnitude defines whether the electrochemical process belongs to either diffusion controlled or capacitive controlled. If "b" value is closer to 0.5, then the electrochemical process is a contribution of diffusion-controlled mechanism (charge storage through Li^+-oxidation/reduction) whereas "b" value 1.0 indicates the capacitance (charge storage via surface capacitance effect).[56,86] The formation of NCO/GQDs compos-

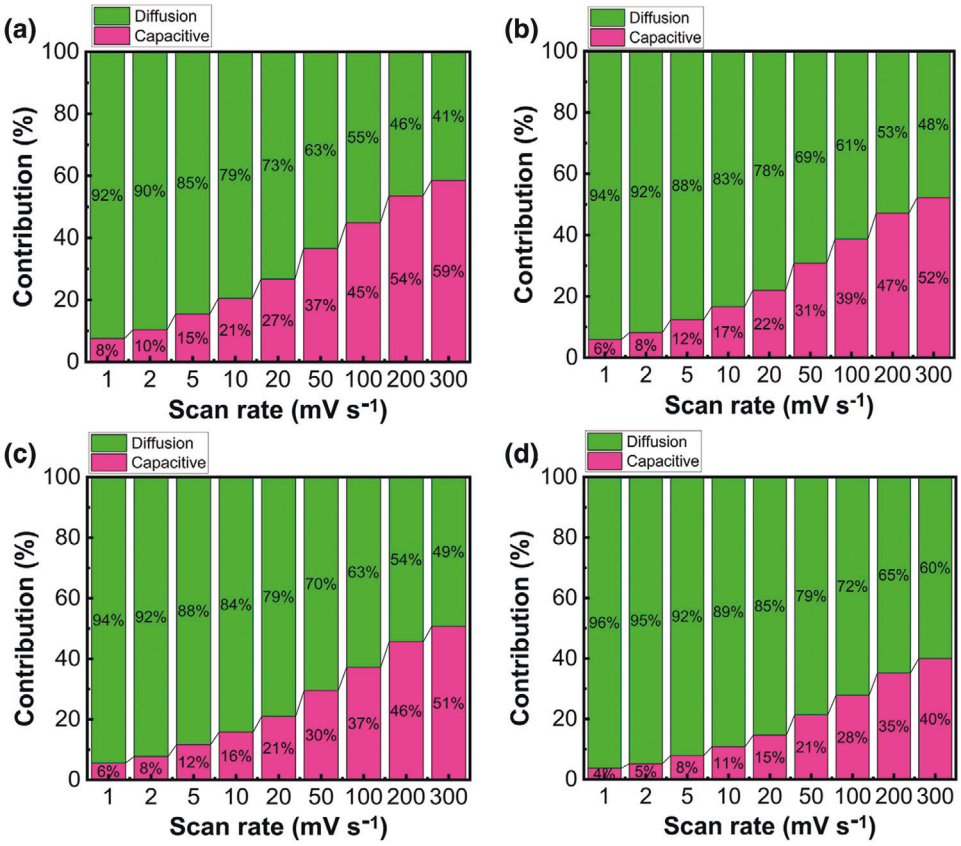

Figure 8. Variation of capacitive and diffusion specific capacitance as a function of scan rate of a) NCOQDs, b) NCO/GQDs-5%, c) NCO/GQDs-10%, and d) NCO/GQDs-15%, respectively.

ite with GQDs and NCO quantum dots with high surface area is responsible for excellent reversibility. The overall contribution of NCO/GQDs −10% electrode under same scan rates is higher than the pristine NCOQDs and other NCO/GQDs nanocomposites. It is worth noting that the high fraction of capacitive contribution can be observed for all the composites over pristine NCOQDs leading to excellent rate capability and fast redox reaction due to the appropriate combination of GQDs with NCOQDs in the composites. The high fraction of capacitance in turn induces cycling stability. The observed quasi-rectangular cyclic voltammetry curves demonstrate a good electrochemical reversibility with low resistance. Further, even at higher scan rates, the quasi rectangularity of CV curves retains their shape, which implies their good electrochemical performance of the electrodes. No observation of O_2 or H_2 gas evolution at the edges of switching potential confirms that these NCO and NCO/GQD-composites have ability to work in the wide potential range without any damage.[86]

Figure 7b,e,h,k shows the log i versus log υ plots at different potentials (0.0–0.5 V). These plots are almost linear for all the electrodes. Also, at all potentials, the b value is between 0.5 and 1.0 for all the samples indicating that the oxidation/reduction of ions dominate for storing charge at all potentials and partly capacitive mechanism involved. It is evident that the current is directly proportional to the square root of scan rate. k_1 (υ) and k_2 ($\upsilon^{1/2}$) represent the capacitive current and diffusion current. The following equation was used to determine these values.

$$i(\upsilon)/\upsilon^{1/2} = k_1(\upsilon^{1/2}) + k_2 \quad (5)$$

where k_1 and k_2 correspond to the slope and intercept of the linear fit of the plot between $i(\upsilon)/\upsilon^{1/2}$ and $(\upsilon)^{1/2}$. After calculating the values of k_1 and k_2, the current contribution can easily be distinguished through diffusion and capacitive mechanism at each potential. The total capacitive behavior with respect to scan rate through diffusion and capacitive process shown in **Figure** 8a–d. Here, the pink color corresponds to the current contribution from capacitive storage while green color relates to the current contribution from diffusion mechanism. These results infer that maximum amount of charge storage occurs via diffusion mechanism rather than capacitive mechanism. This characteristic is congruence to the calculated "b" values from the CV curves. Evidently, at higher scan rates, the diffusion-controlled contribution is gradually decreasing whereas capacitive contribution is gradually increasing. This implies that the electrolyte ions do not have sufficient time to oxidation/reduction process at high scan rate in the NCO matrix. Hence, the electrolyte ions undergo quick adsorption/desorption in addition to oxidation/reduction process near the electrode/electrolyte interface. The diffusion mechanism is more dominant than capacitive mechanism at low scan rate suggesting high specific capacitance of NCO electrode

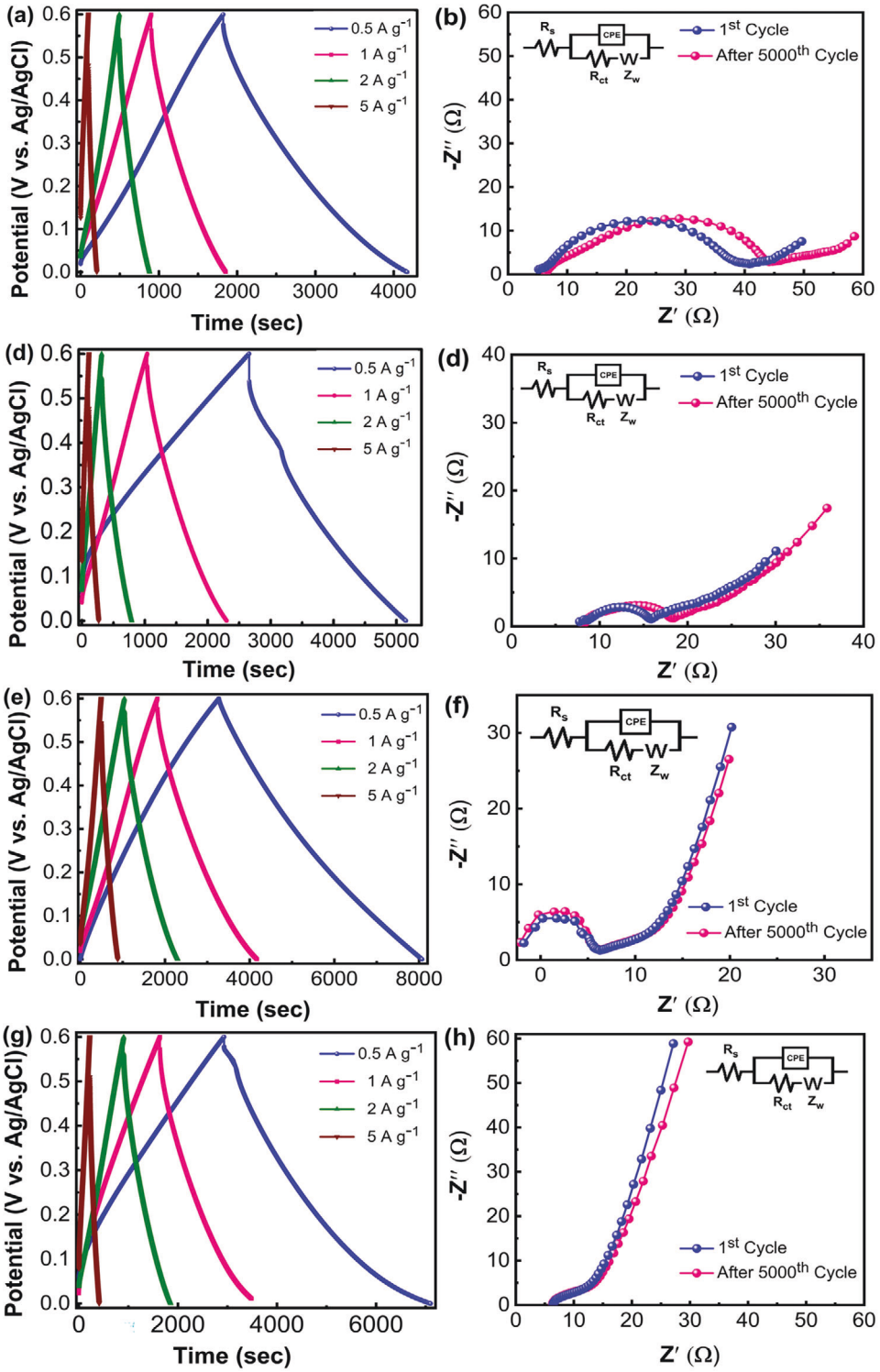

Figure 9. Galvanostatic charge–discharge profiles recorded at different current densities for 0.5, 1, 2, and 5 Ag^{-1} in the potential range of 0.0–0.6 V versus Ag/AgCl, and Nyquist plots of before and after cycling of pristine NCOQDs (a,b) and NCO/GQDs-5% (c,d), NCO/GQDs-10% (e,f) and NCO/GQDs-15% (g,h) nanocomposite electrodes. Inset shows the Randles equivalent electrical circuit that consists of an active electrolyte resistance R_s in series with the parallel combination of the constant phase element CPE_{dl} and an impedance $R_{ct} + Z_w$ of a Faradaic reaction in EIS graphs.

Table 3. The estimated C_s values for all the four electrodes at different current densities.

Electrode	C_s @ 0.5A g^{-1} [F g^{-1}]	C_s @ 1 A g^{-1} [F g^{-1}]	C_s @ 2 A g^{-1} [F g^{-1}]	C_s @ 5 A g^{-1} [F g^{-1}]
NCOQDs	1964	1580	1306	866
NCO/GQDs-5%	2077	2022	1723	1266
NCO/GQDs-10%	3940	3833	3740	3416
NCO/GQDs-15%	3483	3333	2500	2100

originates mainly from pseudocapacitive nature and partially from EDLC nature. The binary metals (Ni and Co) with their synergistic effect contributed more charge, Co can help to improve the electrical conductivity whereas Ni could facilitate more charge storage capability in the NCO unit. The graphene coated on the NCO particles, that not only provide high conductivity but also facilitate mechanical strength by protecting the particles with surface coating could prevent peeling of the electrode material during high charge–discharge rates.

2.3.2. Galvanostatic Charge–Discharge (GCD) Characteristics

The GCD measurements were conducted to evaluate the charge storage ability of all the synthesized compounds in 1 M Li_2SO_4 electrolyte. **Figure** 9a–h depicts the GCD curves and EIS curves (1st and after 5000th cycle) of NCOQDs, NCO/GQDs-5%, NCO/GQDs-10%, and NCO/GQDs-15% electrodes in the voltage range of 0.0–0.6 V at different current densities ranging from 0.5 to 5 A g^{-1}. Among all the electrodes, NCO/GQDs-10% exhibits the longest discharge time demonstrating its superior energy storage ability. Quantum dot morphologies and composition tuning of the most pioneering NCO electrodes are the key factors for their superior specific capacitance. It can be observed that almost triangle-shaped linear and symmetric shape GCD curves are observed at different current densities for all the four electrodes signifying an excellent reversibility of forward and backward reactions elucidate another characteristic of pseudocapacitive behavior that is in accordance with the CV results and analyses. The symmetric behavior of GCD curves suggests good reversibility of NCO/GQDs composite electrodes. The IR drop is negligible at the beginning of the discharge time even at high current density ascribed that the electrode material has low internal resistance with lower energy loss. The low pore size and large pore volume of the material act as an ion-buffering reservoir and help to improve the conductivity, reversibility as well as ion/electron kinetics by reducing the anions mean free path.[53] The C_s can be calculated using the following equation:

$$C_s = \frac{I\Delta t}{m\Delta V} \tag{6}$$

where "C_s" is the specific capacitance (in F g^{-1}), "I" is the charge/discharge current, "Δt" is the time of discharge, "ΔV" is the voltage difference between the upper and lower potential limits and "m" is the mass of the active material. The estimated C_s values for all the four electrodes at different current densities are listed in **Table** 3.

It can be observed that (Table 3), with increasing current density, the C_s values decrease. The lower C_s values obtained at high currents are mainly attributed to volume expansion corresponding to repeated multi-electron electrochemical reactions. NCO demonstrates the cubic spinel structure in which Ni atoms are located at octahedral sites whereas Co is situated in both tetrahedral and octahedral sites. Two cations (Ni,Co) participated in the redox reactions with their corresponding sites (tetrahedral sites of Ni) and both (tetrahedral and octahedral sites of Co) and contribute their oxidation states is the major reason for high specific capacitance of NCO compounds. It can be observed that specific capacitance of NCO composites is more than the C_s of pristine NCOQDs implies that the Ni active sites are more in NCO/GQDs composites. The O 2p and 3d holes (orbital) of Ni/Co have strong ligand–metal bond in the structure. During charging/discharging, the electronic structure of this bond is highly reversible. Generally, the oxygen containing functional groups on the surface of the NCO composite can reversibly transform through faradaic and non-faradaic reactions that proceed close to material surface, it could help to form robust oxygen –carbon brides that leads to metal-to-ligand charge transfer at the interface between NCO and GQDs.[57] Hence, NCO composites could be able to provide rich redox sites and improve their electrochemical performance with the combination of both pseudocapacitance and electrical double layer nature. The redox changes during charging and discharging acceleration excellent transport of electron/ion and improving the pseudocapacitive nature with enhanced electrochemical reactions.

2.3.3. Mechanism

In $NiCo_2O_4$ inverse spinel crystal structure the oxygen anions connect with CO_4 tetrahedra and Ni/CoO_6 octahedra.[84,85] The versatile applications of NCO are determined by its crystal structure with mixed valence states of +2 for Ni and +3 for Co cations. Half of the Co-ions can occupy in T_d–site (tetrahedral) whereas other half of Co/Ni ions can be occupied in the O_h – sites (octahedral) to form "Nickel Cobaltite," which offers rich redox chemistry. The calculated lattice parameter of NCO is 8.10 Å. Based on the metallic characteristic, NCO demonstrates half metal in which the majority spin channels possess insulating behavior. Whereas minority channels become conductive in nature. The Ni (O_h) and Co (T_d) give high conductivity in the compound. In both the spin channels of Ni and Co valance band toward Fermi level, precisely the Ni^{2+} in place of Co^{3+} at an octahedral (O_h) site act as *p*-type dopant. This Ni^{2+} (O_h) causes to form Co^{3+} tetrahedral (T_d) that contains one occupied e-orbital in the minority spin channel. Therefore, a hole can be generated on the top of the valance band due to another Co (T_d) empty e-orbital. In the counterpart, Ni^{3+} (O_h) site results Co^{2+} (T_d) with an empty e^g – state causes a hole at the top or just above the valance band. In these two cases empty states are formed at the top of the minority spin valance band that leads to high conductivity to the NCO sample. Later the Ni (O_h) and Co (T_d) sites crossed the Fermi level in the spin–down channel.[58] It reveals that Ni (O_h) and Co (T_d) exchange interaction improves the conductivity in NCO and, hence, an enhancement in the specific capacitance. During the discharge process,

the Li^+ ion insertion may occur at the Ni^{3+} (O_h) and Co^{2+} (T_d) sites. At these two particular sites (throughout the cell), the distance between O (2p) and Ni is 1.95 Å, while the bond length between Co—O (tetrahedral) is 1.98 Å and the bond length between Co^{3+}-O (2p) is 1.89 Å (octahedral) is comparatively less than other Ni—O and Co—O bond length in the different place. As a result, Li^+-ion proceeds with insertion into the Ni^{3+} (O_h) site and Co^{2+} (T_d) sites initially and later into the other sites.[42] During charging, the Li^+-ion extraction occurs from the Co^{2+} (T_d) and Ni^{3+} (O_h) sites later in the rest of the sites. This completes the charge–discharge cycle in NCO. The following conclusions derived from the abovementioned electrochemical mechanism. First, the large electronic state contribution from octahedral Co, Ni, and tetrahedral Co of NCO near the Fermi level provides more charge carriers for faradaic redox reactions, which leads to accelerate the redox activities. Second, surface dynamics such as easy and quick (anion) insertion and deprotonation process can accelerate the overall electrochemical process. Third, the synergistic effect of both Co and Ni in addition to conductive GQDs helps to improve the reaction activity.[33] Fourth, the surface of NCO with high concentration of active redox sites including higher electron supply capability causes a large degree of oxidation after reaction. Moreover, it can be observed that specific capacitance of NCO composites is more than the C_s of pristine NCOQDs that the Ni active sites are more in NCO/GQDs composites. The O 2p and 3d holes (orbital) of Ni/Co have strong ligand–metal bond in the structure. During charging/discharging, the electronic structure of this bond is highly reversible. Generally, the oxygen containing functional groups on the surface of the NCO composite can reversibly transform through faradaic and non-faradaic reactions that proceed close to material surface, it could help to form robust oxygen–carbon brides that leads to metal-to-ligand charge transfer at the interface between NCO and GQDs.[81] Hence, NCO composites would be able to provide rich redox sites and improve their electrochemical performance with the combination of both electrical double layer and pseudocapacitance nature. After introduction of GQDs into NCO structure, a strong interaction of C–O–Ni/Co can suggestible between NCO and GQDs, which creates plenty of exposed redox active sites. The C–O–Ni/Co strong interactions not only provide highly conductive channels as effective electron/ion paths but also change the local structure and oxidation changes of Ni^{2+} to Ni^{3+} and Co^{2+} to Co^{3+}.[43] GQDs interact with NCO molecules though π–π stacking electrostatic interaction, and chemical bonding resulting in coating of the GQDs on the NCO framework. Stable free radicals are known as pseudocapacitance quenchers and are used in this work to improve pseudocapacitance. The one-half distance between the nuclei of NCO and GQDs in a NCO/GQDs composite is called van der Walls distance. The van der Walls bond between the NCO and GQDs is weaker than the Ni-Co metallic bond, but the GQDs give mechanical stability to NCO framework. The introduction of GQDs into NCO framework is lowering the band gaps of NCOQD's as a result electron density has increased with the SP^2 clusters of graphene layer that may improve the electrical conductivity. The van der Walls distance of the NCOQDs and GQDs compounds reduced after forming as composite that facilitates lowering the band gaps in NCOQDs, that leads to improve the electrical conductivity to the electrode. The redox changes during charging and discharging acceleration excellent transport of electron/ion and improving the pseudocapacitive nature with enhanced electrochemical reactions. The NCO has appealing congenital advantages and reasonably anticipated with even better electrochemical performance than the other supercapacitor materials.

A series of experimental results delineates that the electrochemical performance improvement in NCO/GQDs can be attributed to the following features:

i. Both NCOQDs and GQDs demonstrate excellent pseudocapacitive nature in the same electrolyte.
ii. The dispersion of quantum dots in the graphene sheets could shorten the solid-state pathways for ion diffusion along with prompt charge transfer.
iii. The NCOQDs have reliable electrical connection to graphene causes to construct a reliable 3D-channels conductive channels for rapid transport all over the electrode that caused to maximum harvest of pseudocapacitance from both NCO and graphene is prompted.
iv. The mesoporous nature and high pore volume of nanocomposite produce additional channels for electrolyte infiltration and formed rich redox sites that can be accessible easily in high quantity to the electrolyte ions.
v. The combination of NCO and graphene would ample a robust synergistic effect and excellent mechanical integrity for enhancing the energy storage capability.

All these advantages enable the NCO/GQDs to exhibit outstanding properties such as exceptional specific capacitance, long calendar life and prior rate capability are highly desirable qualities for supercapacitor implementations.

2.3.4. Electrochemical Impedance Spectroscopy (EIS)

To understand the ion diffusion and charge transfer process, NCO/GQD nanocomposites were characterized by electrochemical impedance spectroscopy (EIS). The EIS measurements were carried out in the frequency range of 1 Hz to 1 MHz at a bias voltage of 5 mV before and after the cycling stability test. The data obtained are shown in Figure 9b,d,f,h. As shown in Figure 9b,d,f,h, EIS spectra of all the samples composed of three parts. The obtained Nyquist plot is extrapolated at high frequency to touch real impedance (X-axis) is ascribed ohmic (uncompensated) resistance (R_s), which generally originated by ionic resistance of the electrolyte. The semicircle originated from high to low frequency region corresponds to charge transfer resistance (R_{ct}), which is attributed to electronic resistance of the electrode materials and contact resistance of electrode/electrolyte interface. The straight line derived at low frequency region represents Warburg impedance (W_z). The diameter of semicircle corresponds to charge transfer resistance (R_{ct}) at the electrode/electrolyte interface. All the EIS spectra consist of one semicircle in the high frequency and a straight line at low frequency region simulated by equivalent circuit. The EIS spectra straight line at low frequency region demonstrates the slope is approximately >45° suggesting the capacitance for all the four electrodes is controlled by electrolyte ion diffusion process.[61] As shown in Figure 9b,d,f,h, the pristine NCOQDs shows a large semicircle diameter at high frequency region implies high impedance

Table 4. The R_{ct} and R_s values of before and after cycling test of all the NCO/GQDs electrodes.

	NCO		NCO/GQD-5%		NCO/GQD-10%		NCO/GQD-15%	
	R_s	R_{ct}	R_s	R_{ct}	R_s	R_{ct}	R_s	R_{ct}
1st cycle	5	40	7	15	1	4	6	11
After 5000th cycle	6	44	8	18	1	6	7	13

for both before and after cycling tests due to quantum dots of NCO are only participated to accelerate electron/ion transfer. After inculcation of GQDs into NCO structure, the impedance is reduced. The semicircle diameter of NCO/GQDs composite is comparatively low in both cases before and after cycling test over pristine NCOQDs resulting low impedance and low electron transfer resistance due to incorporation of GQDs in NCO. The GQDs provide unique architecture between NCOQDs and graphene sheets and enhance the electrical conductivity and high surface-active sites. The corresponding charge transfer resistance (R_{ct}) value of NCOQDs and NCO-GQDs composite electrodes are in the following order NCOQDs>NCO/GQD-5%>NCO/GQD-15%>NCO/GQD-10% respectively. The R_{ct} and R_s values before and after cycling test of all the four electrodes are listed in **Table 4**. Among them, NCO/GQD-10% composite displays very low diameter of semicircle compared to other two electrodes indicating that NCO/GQD-10% possess very low resistance (4 Ω) and high electron transfer rate. The synergistic effect of Ni-Co will accelerate the ions from the binary metal (NCO) oxide. Moreover, the GQDs enhance the conductivity to the NCO compound after successful coating. Due to these two strong reasons semi-infinite diffusion is more dominant in charge storage mechanism. The mesoporous structure of NCO/GQDs can ameliorate wettability between the material and ions of the electrolyte resulting in improved conductivity by reducing charge transfer resistance, which leads to high pseudocapacitance.

The Trassati equation was used to find the amount of specific capacitance contributed from inner and outer surface of the NCO/GQDs-10% electrode at a scan rate of 300 mV s^{-1}. The data obtained are shown in **Figure 10a**. Trassati expressed that the total specific capacitance provided by inner and outer surface of the electrode as:

$$C_{total} = C_{in} + C_{out}\ (Fg^{-1}) \tag{7}$$

The specific capacitance contributed from inner and outer surface of the electrode depends upon the scan rate (υ).[83] The estimated specific capacitance of NCO/GQDs-10% electrode at a scan rate of 300 mV s^{-1} total outer and inner surface is 2114 and 1313 Fg^{-1}, respectively. In that, the inner surface of electrode has high number of redox active sites over outer surface due to the redox reactions of ions. To further study the cycle stability and durability of synthesized intrinsic NCOQDs and NCO/GQDs composites, stability tests were made by repeated charge–discharge measurements. The results are displayed in Figure 10b, where the cycle stability of intrinsic NCOQDs and NCO/GQDs composites at a current density of 1 Ag^{-1} are shown. All the electrodes (NCOQDs, NCO/GQDs-5%, NCO/GQDs-10% and NCO/GQDs-15%) demonstrate specific capacitance of 1580, 2022, 3833, and 3333 F g^{-1} and retained capacitance of 92%, 94%, 98%, and 96% (1453, 1920, 3753, and 3233 Fg^{-1}) at 1 Ag^{-1} after 5000 cycles. The reason for capacitance fading in intrinsic NCOQDs is due to dissolution of material into electrolyte. The lesser capacitance fading has been observed for NCO/GQDs composites owing to bonding between graphene and NCO in the composite becomes weak and the shrinkage of graphene sheets. The mechanical stress upon the electrode during charge–discharge process is another strong reason for capacitance fading.[60] Figure 10c shows the variation of C_s with different current densities for all the electrodes. It shows that at low current density, the diffused ions of the electrolyte have high redox reaction tendency, which causes occupation of plenty of electrochemically activation sites throughout the surface of the electrode leads to extensive charge storage. Moreover, the diffusion ions of the electrolyte have sufficient time to diffuse in the active material and access almost all active sites that are possibly available inside and the bulk of the material. Whereas the outer surface sites can be involved in electrochemical reactions at high current densities resulting in relatively lower specific capacitance. All the electrodes exhibit lower specific capacitance at higher scan rates infers that the specific capacitance of the electrode material highly

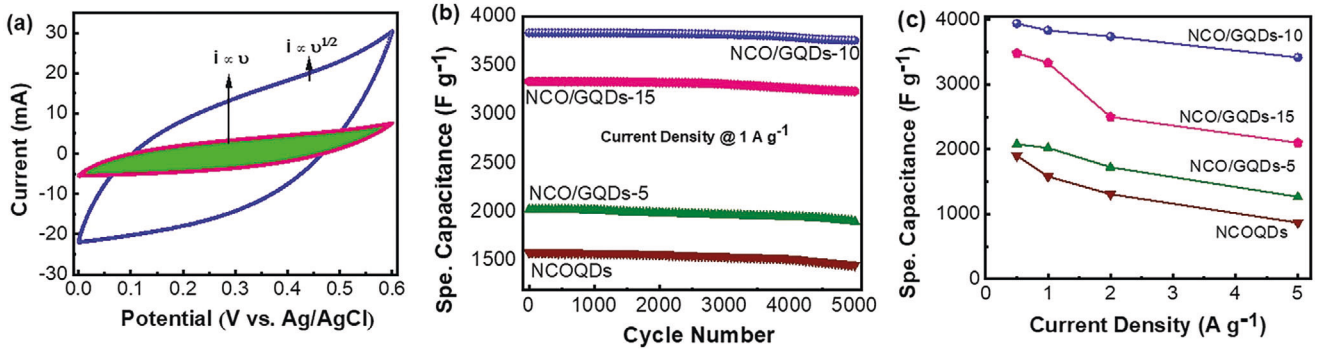

Figure 10. a) Comparative total current obtained experimentally (solid line) and capacitive current (shaded area) of NCO/GQDs-10% nanocomposite, b) Specific capacitance versus cycle number of electrodes tested at 1 Ag^{-1} and c) variation of specific capacitance as a function of current density of NCOQDs and NCO/GQDs with variable GQDs concentration.

depends on the current density. The excellent capacitance retention of NCO/GQDs-10% composite is attributed to the unique mesoporous structure that could alleviate volume expansion during charge–discharge process. Based on the results and analyses thus far, the NCO/GQDs-10% composite electrode demonstrated excellent structural and electrochemical properties; it delivered a high C_s of 3833 Fg^{-1} at 1 Ag^{-1} and retained 98% of capacitance after 5000 cycles. Mean free path refers to the average distance that a moving particle travels between successive collisions results in modification of the moving particles energy or direction or any other particle properties. The quantum dot size NCO/GQDs particles is to shorten the Li^+ – ion diffusion path and the GQDs will provide more conductivity to the electrode. With these benefits the anion mean free path can be reduced that provide excellent supercapacitor performance and reversibility of the ion/electron kinetics by reducing the anion mean free path. The electrochemical performance of various NCO based electrodes are shown in **Table 5**. Based on the material and electrochemical characterization outcomes leaning toward NCO/GQDs-10% composite as the most favorable electrode, it is taken as an active electrode to further study the performance of the asymmetric supercapacitor (ASC) and symmetric supercapacitor (SSC) devices.

Comparison with NCO/GQDs

2.4. Supercapacitor Device Performance Characteristics and Evaluation

2.4.1. NCO/GQDs-10%//AC Asymmetric Supercapacitor (ASC) Device

To further evaluate the practical applications of NCO/GQDs, we designed and fabricated the supercapacitor devices and studied their performance. The NCO/GQDs-10% electrode for energy storage rechargeable asymmetric supercapacitor (ASC) configuration is constructed using two electrode pouch type devices. The supercapacitor device was fabricated by the NCO/GQDs-10% electrode as positive electrode whereas activated carbon (AC) used as negative electrode and PVA/KOH gel electrolyte was used as an ion-conductive channel, a whatman filter paper can be used as a separator to prevent direct contact in the device. The schematic diagram of the device constructed is shown as **Figure 11a**.

Figure 11b shows the typical cyclic voltammogram (CV) curves of ASC device at different scan rates ranging from 1 to 100 mV s^{-1} for the NCO/GQDs-10%//AC device. It can be observed that NCO/GQDs-10%//AC device demonstrates a clear and broad oxidation peak at 1.2 V and the reduction peak at 0.63 V indicating that both NCO/GQDs-10% and AC equally contribute their inherent storage characteristics. The CV curves obtained are similar for all the scan rates (1–100 mV s^{-1}). Apparently,

Table 5. Comparison of the electrochemical performance of NCO/GQDs electrode materials.

Electrode materials	Method	Potential window [V]	Current density [mAg^{-1}]	Electrolyte	Specific capacitance [$F\ g^{-1}$]	Capacity retention [%]	Refs.
$NiCo_2O_4$/GQDs (10%)	Hydrothermal method	0.0–0.45	1000	1 M KOH	302	87 (1000)	[43]
$NiCo_2O_4$QDs	Hydrothermal method	−0.9–0.9	500	1 M Na_2SO_4	362	86 (1000)	[15]
CQDs/$NiCo_2O_4$	Reflux synthesis route	0.0–0.5	1000	2 M KOH	856	98 (10 000)	[32]
Tremella like $NiCo_2O_4$@GQDs	Hydrothermal method	1.0–3.0	30 000	2 M KOH	1242	99 (4000)	[42]
$NiCo_2O_4$/GQDs	Solvothermal and Hydrothermal method	0.0–0.45	1000	0.1 M KOH	1238		[62]
$NiCo_2O_4$/GQDs	Solvothermal and Hydrothermal method	0.0–0.45	30 000	0.1 M KOH	1242	99 (4000)	[63]
$NiCo_2O_4$/GQDs	Solvothermal and Hydrothermal method	0.0–0.45	350	0.1 M KOH	481	65 (300)	[27]
	Solvothermal method	0.0–0.55	10 000	6 M KOH	1361	76.4 (3000)	[33]
N-CQDs/Co_3O_4	Hydrothermal method	−1	1000	6 M KOH	1867	96 (5000)	[64]
NCONA/ Carbon cloth	Hydrothermal method	0.0–0.5	2000	2 M KOH	660	91.8 (3000)	[86]
NCOQDs$_5$-rGO$_{1.5}$	Hydrothermal method	−0.2–0.4	730	1 M Na_2SO_4	265	96 (1000)	[33]
Ni/NCO/RGO	Solvothermal and Hydrothermal method	0.0–1.6	-	1 M Li_2SO_4	253 F/cm3	81 (5000)	[48]
$NiCo_2O_4$/RGO				1 M KOH	737	94 (3000)	[87]
$NiCo_2O_4$@PPy NWAs	Hydrothermal method	0.1–0.6	3000	3 M KOH	2244	82.9 (10 000)	[25]
$NiCo_2O_4$QDs	Hydrothermal method	0. 0–0.6	1000	1 M Li_2SO_4	1580	92 (5000)	this work
$NiCo_2O_4$/GQDs (5%)	Hydrothermal method	0. 0–0.6	1000	1 M Li_2SO_4	2022	94 (5000)	this work
$NiCo_2O_4$/GQDs (15%)	Hydrothermal method	0. 0–0.6	1000	1 M Li_2SO_4	3333	96 (5000)	this work
$NiCo_2O_4$/GQDs (10%)	Hydrothermal method	0. 0–0.6	1000	1 M Li_2SO_4	3833	98 (5000)	this work

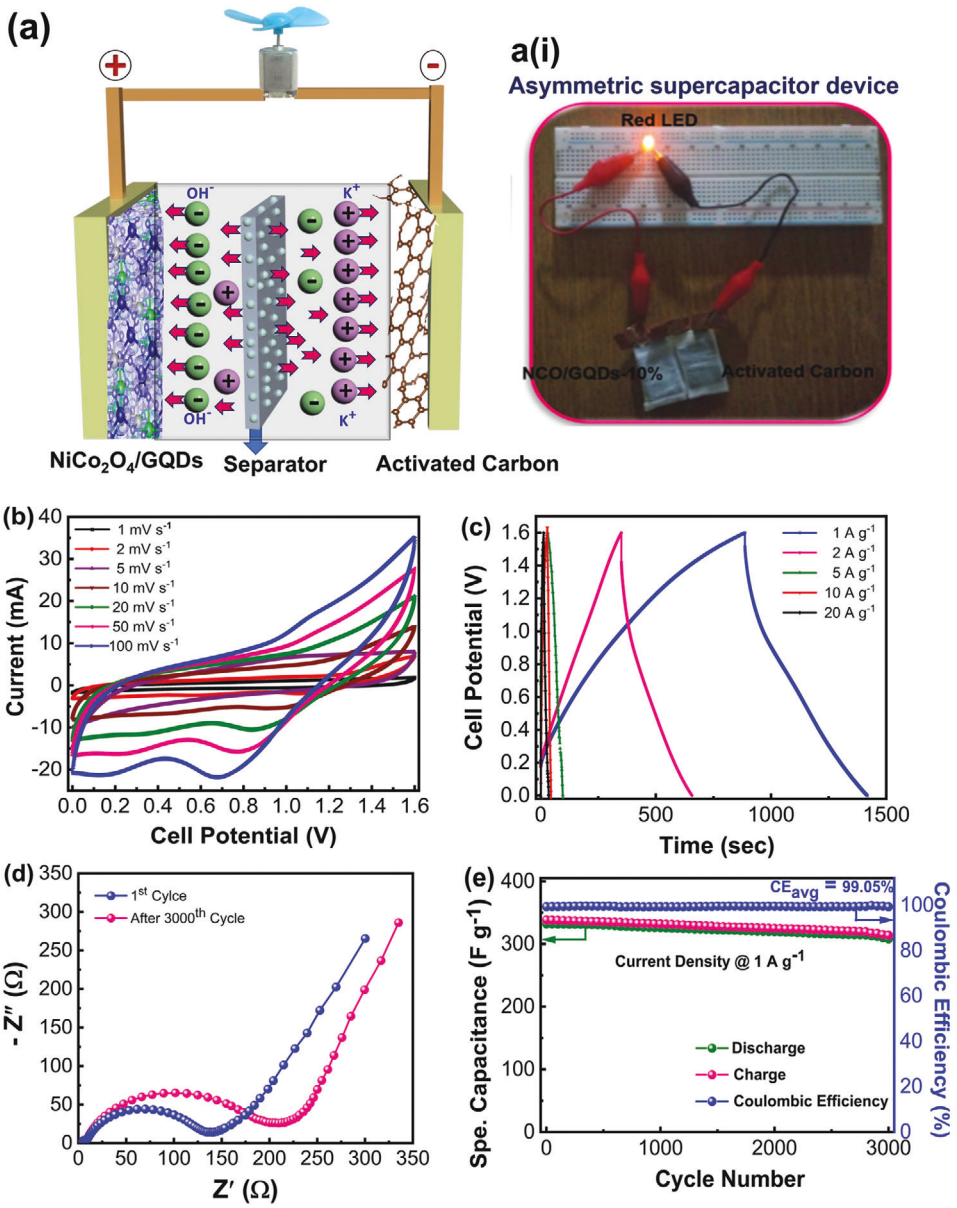

Figure 11. Schematic diagram of NCO/GQDs-10%//AC asymmetric supercapacitors (ASC) fabricated and their electrochemical performance characteristics. a) Schematic diagram of the ASC device. a(i). photograph of red LED illumination using NCO/GQDs-10%//AC ASC device, b-e) Electrochemical properties of NCO/GQDs-10%//AC asymmetric supercapacitor (ASC) in the potential range 0.0–1.6 V pouch cells. The data shown are: Cyclic voltammograms recorded at scan rate range of 1–100 mV s^{-1} (b), Galvanostatic charge–discharge (GCD) curves cycled at various current densities of 1–20 A g^{-1} (c), Nyquist plots (before and after cycling) in the -Z'' versus Z' plane (d), and Specific capacitance and Coulombic efficiency versus cycle number of electrodes tested at 1 A g^{-1} (e).

each CV profile consist of symmetrical oxidation/reduction peaks that are corresponding to the reversible Faradaic redox reactions of Ni^{2+}/Ni^{3+} and Co^{2+}/Co^{3+} inferring that capacitance of NCO/GQDs-10%//AC mostly attributed to the redox pseudocapacitance along with EDLC.[88] With increasing scan rate from 1 to 100 mV s^{-1}, the CV profile current density and integral area under the CV curves increased indicating good rate kinetics of the device and redox reactions are diffusion controlled. With excellent reversibility at all sweep rates from 1 to 100 mV s^{-1} in the potential window of 1.6 V signifies good charge propagation within the electrodes. Moreover, for all the CV profiles, no distinct or shape distortion is observed at high scan rates illustrating a favorable rate capability and reversibility, which is ascribed to effective ionic and electronic transmission in the electrode material.

The galvanostatic charge–discharge measurements are carried out to further explore the electrochemical performance of the ASC device. Figure 11c demonstrates GCD curves of NCO/GQDs-10%//AC ASC at different current densities ranging from 1 to 20 A g^{-1} within the potential cutoff 0.0–1.6 V.

It can be observed that one pair of nonlinear increase and decrease of the potential with respect to time in GCD curves are observed for device ascribed pseudocapaitive characteristic. The non-linear increase and decrease of the potential with a modest IR drop are attributed and evidence of perfect capacitive behavior of the device and corroborates to CV profile.[89] With increasing current density, the reduction in the specific capacitance can be observed for the ASC device signifying that the ASC devices have a good rate capability. The NCO/GQDs-10%//AC device shows highest discharge time at a current density of 1 Ag^{-1} indicating that its high conductivity that leads high specific capacitance. The NCO/GQDs-10%//AC ASC device demonstrated excellent discharge time indicating it could be able to deliver an excellent energy density and power density. The NCO/GQDs-10% provides high surface area and large pore volume that can act as ion buffering reservoirs that play predominant role to improve the reversibility by reducing the anions mean free path by facilitating the rapid ionic and electronic kinetics.[90] The device delivered specific capacitance of 332, 312, 212112, and 150 Fg^{-1}, respectively, at different current densities of 1, 2, 5, 10, and 20 A g^{-1}. The NCO/GQDs-10%//AC ASC device showed excellent specific capacitance due to its special morphology with graphene architecture that connected NCOQDs as a result it demonstrates high energy density (E) of 118.04 Wh Kg^{-1} and an excellent power density (P) of 798.76 W Kg^{-1}, respectively. The NCOQDs have reliable electrical connection to graphene causes to construct a reliable 3D-channels conductive channels for rapid transport all over the electrode that caused to maximum harvest of pseudocapacitance from both NCO and graphene is prompted. Due to the successful graphene coating over the NCOQDs can not only give high mechanical stability to the electrode but also avoid peeling of the material during charge–discharge process at high rates. The E and P values obtained are better than the reported E and P values of many reports in the literature. Poonam et al. reported that the ASC device constructed with NCOQDs and rGO as positive and negative electrodes. The NCOQDs//rGO demonstrated a better energy density of 69.5 Wh kg^{-1} and a power density of 2.2 kW kg^{-1}.[15] The asymmetric supercapacitor fabricated by Zhu et al. using carbon quantum dots (CQDs) tuned porous $NiCO_2O_4$ sphere and Activated carbon (AC) as positive and negative electrodes, the AC//CQDs/$NiCo_2O_4$ manifest a high energy density of 27.8 Wh kg^{-1} and a power density of 128 W kg^{-1}.[32] Luo et al. constructed an ASC by pairing a tremella like $NiCo_2O_4$@GQDs composite and AC as a positive and negative electrodes and $NiCo_2O_4$@GQDs//AC showed a good energy density of 38 Wh kg^{-1} and a power density of 800 W kg^{-1}.[42] Asymmetric supercapacitor (ASC) device is fabricated by Arvind Singh et al. using $NiCo_2O_4$@$MnMoO_4$ core@shell nanoarrays. The fabricated device demonstrated a high energy density of 91.87 Wh kg^{-1} at power density of 374.15 W kg^{-1}.[90] Yin et al. assembled all-solid-state ASC using NiO@Co_3O_4@GQDs and AC, it exhibited a maximum energy density of 38.44 Wh kg^{-1} with good cycle stability.[34] Kong et al. reported that the ASC device of AC//$NiCO_2O_4$@PPy NWAs performed a good energy density of 58.8 Wh kg^{-1} and outstanding power density of 10.2 KW kg^{-1} respectively.[25] In another work Poonam et al. assembled supercapacitor using NCOQDs-rGO as positive and negative electrodes, where the device delivered an energy density of 47 W h kg $^{-1}$ and a power density of 631 W kg $^{-1}$ within a wide potential window of 1.6 V.[33] An ASC was assembled by Li et al. using hydrogenated $NiCo_2O_4$ double shell hollow sphere and AC as positive and negative electrodes. This NCO//AC device showed an energy density of 34.8 W h kg^{-1} and a power density of 464 W kg^{-1}, respectively.[91] Khalid et al. fabricated an ASC using porous $NiCo_2O_4$ and AC and this $NiCo_2O_4$//AC device demonstrated maximum areal capacitance and energy density of 380 mF cm^{-2} & 19.1 Wh kg^{-1} at current density of 1 mA cm^{-2}.[58] Zhao et al. reported that the ASC device constructed with Sic@Fe_2O_3 nano needle arrays (Fe_2O_3 NNAs) and mesoporous Sic@ $NiCo_2O_4$@$Ni(OH)_2$ positive electrode on carbon cloth (CC). It demonstrated a better energy density of 103 Wh kg^{-1} and a power density of 3.5 KW kg^{-1} and it showed long cycle span of 86.6% capacitance after 5000 cycles.[80] The asymmetric supercapacitor fabricated using $NiCo_2O_4$ nanoparticles on 3D graphene (3D-G) as positive and negative electrodes and it delivered a high energy density of 73.8 Wh kg^{-1} and a power density of 800 W kg^{-1} with a long cycle stability 94.3% capacitance retention after 5000 cycles reported by Sun et al.[39] Deen et al. fabricated ASC using uniform distribution of $NiCo_2O_4$ nanorods anchored on carbon nanofibers as a positive electrode and activated multichannel carbon nano fibers (AMCNFs) as a negative electrode.[40] Chu et al. constructed an ASC using phosphorous doped $NiCO_2O_4$ nano wires on nickel foam (P-NCO NWs/NF) as a positive electrode, rGO as a negative electrode. The P-NCO NWs/NF//rGO ASC configuration demonstrated an energy density of 28.2 Wh kg^{-1} even at a high-power density of 7750.35 W kg^{-1}.[92]

Figure 11d depicts the electrochemical impedance spectroscopy (EIS) for the assembled ACS device. The EIS data demonstrate similar character peaks before and after cycling including small semicircle arc from high to medium frequency region corresponding to charge transfer resistance followed by a straight line. EIS is done in the frequency range of 1 Hz–1 м Hz at amplitude of 5 mV. The Nyquist plot consists of three parts. A semicircle at high frequency region related to charge transfer resistance (R_{ct}) showing interior C_s. At low frequency region, a slope of the Nyquist plot tends to a vertical asymptote signifying electrolyte diffusion (Warburg) impedance. The vertical line with slope of > 45° inferring that capacitance is controlled by ion diffusion process. The estimated lower R_{ct} value of 148 Ω for NCO/GQDs-10%//AC device causes accumulation of charge storage, which is more in NCO/GQDs-10%. The NCO/GQDs-10% have 2D graphene sheets that could store excellent energy even at high current rates. After 3000 cycles, the R_{ct} values were increased to 220 Ω due to the mechanical stress on the electrode during the charge/discharge process. The achievement of high performance is critical factor regarding the practical application of the device is primarily determined by high mass loading of the material.[93] The stability and long-term usage of the device is determined by cyclic stability test. The cyclic stability test was performed at 1 Ag^{-1} to explore the endurance of ASC device for a long-time usage. Figure 11e shows cycle stability versus coulombic efficiency of the ASC device at a current density of 1 Ag^{-1}. The C_s of the device demonstrates 332 Fg^{-1} and retained a C_s of (308 Fg^{-1}) 93% even after 3000 cycles. The capacitance retention is exceptional; it is better than many of the reported ASC devices in the literature. The obtained capacitance fading for the ASC device during cycle test may be due to the mechanical stress on

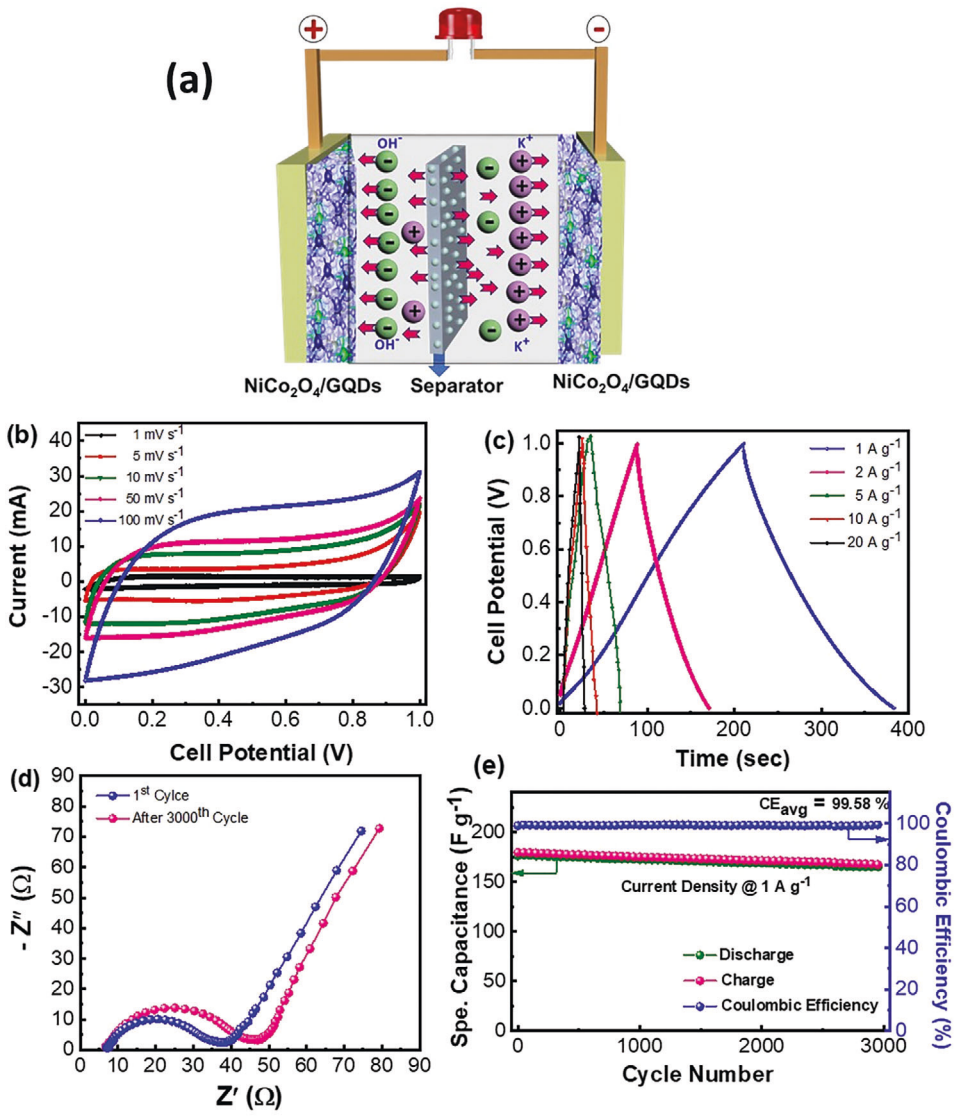

Figure 12. Schematic diagram of NCO/GQDs-10%// NCO/GQDs-10% symmetric Supercapacitor devices fabricated and their electrochemical performance characteristics. a) Schematic of the symmetric supercapacitor. b–e) Electrochemical performance characteristics of the NCO/GQDs-10% symmetric supercapacitor (SSC) in the potential range 0.0–0.1 V. The data shown are: Cyclic voltammograms recorded at scan rate range of 1–100 mV s^{-1} (b), Galvanostatic charge–discharge (GCD) curves cycled at various current densities of 1–20 Ag^{-1} (c), Nyquist plots (before and after cycling) in the Z' versus -Z'' plane (d), and Specific capacitance and Coulombic efficiency versus cycle number of electrodes tested at 1 Ag^{-1} (e).

the electrode material during insertion/deinsertion of electrolyte ions during cycling process. The reversibility of ASC device was further explored by measuring the coulombic efficiency shown in Figure 11e. The ASC device demonstrates excellent coulombic efficiency of 99.05% for 3000 cycles, which represents a higher degree of reversibility.

2.4.2. NCO/GQDs-10%//NCO/GQDs-10% Symmetric Supercapacitor (SSC) Devices

To explore the ability and reliability of NCOQDs based electrodes for symmetric supercapacitors, and similar to ASC devices, the symmetric supercapacitors were designed and fabricated using similar electrodes as positrode and negatrode. The symmetric device of NCO/GQDs-10% was fabricated with two similar electrodes of NCO/GQDs-10%. The symmetric device (**Figure 12**a) of NCO/GQDs-10% was fabricated in the same way as that used for asymmetric device.

Figure 12b–e depicts the electrochemical performance characteristics of SSC devices. Figure 12b displays the CV profile of NCO/GQDs-10%//NCO/GQDs-10% SSC device at different scan rates ranging from 1 to 100 mV s^{-1} in the potential window 0.0–1.0 V in the PVA+KOH gel electrolyte. The CV profile of NCO/GQDs-10%//NCO/GQDs-10% demonstrated almost rectangular shaped curves indicating pseudocapacitive nature contributed by Faradaic reactions along with non-Faradaic EDLC behavior that can be attributed to Ni^{2+}/Ni^{3+} and Co^{2+}/Co^{3+}.[27] With

increasing scan rate, the shape of the CV profile is similar and retaining the same shape without distortion that could be attributed to the lack of restriction of mass transfer and ion transport of charges between the electrode and electrolyte, which is an indication of kinetic reversibility of symmetric device. The cyclic voltammetry (CV) NCO//NCO symmetric supercapacitor demonstrated quasi-rectangular peaks that is the combination of pseudocapacitance and EDLC behavior of electrode. At low scan rates (0.5 mA g^{-1}), there might be a possibility of broad oxidation/reduction peaks. At high scan rates, the electrolyte ion does not have sufficient time store charge so unable to find clear oxidation/reduction peaks. Where in ASC, the activated carbon with high surface area and pseudocapacitive behavior of NCO/GQDs provoke the dominance of pseduocapacitive behavior so we can observe clear oxidation/reduction peaks at their corresponding potential values. The galvanostatic charge–discharge curves of the NCO/GQDs-10%//NCO/GQDs-10% based symmetric device is shown in Figure 12c. The GCD curves of the NCO/GQDs-10%//NCO/GQDs-10% SSC device is carried out with different current densities ranging from 1 to 20 Ag^{-1}, respectively, within the potential window of 0.0–1.0 V. The data are shown in Figure 12c, where almost symmetrical GCD curves with small voltage drop at their initial stage of discharge ascribed pseudocapacitive and double layer capacitance characteristics of good conductive nature of symmetric device. The specific capacitance of the SSC device can be calculated using the mass balancing of the active materials at current densities of 1,2,5 10 and 20 Ag^{-1} respectively. The capacitance (C_s) of full cell SSC device is 175, 160, 150, 120, and 60 F g^{-1} at different current density of 1, 2, 5, 10, and 20 Ag^{-1} respectively. At low current density, the ions in the electrolyte completely react with the active material endures great improvement in the utilization of electrode active material. At high current density, the ion insertion/extraction process is very fast and unable to access the complete area of the electrode. So, charge on the electrode surface was not established well compared with low current rates. The obtained GCD curves at different current densities remained symmetric and unchangeable demonstrating that the NCO base SSC device is very reliable at high current rates. The NCO/GQDs-10%//NCO/GQDs-10% SSC device demonstrates a high energy density of 24.30 Wh kg^{-1} and excellent power density of 500 W kg^{-1}, respectively, these excellent values indicating the superior device performance comparing with many reported SSC of NCO/GQDs devices.

Electrochemical impedance spectroscopy (EIS) of SSC device (before and after cycling tests) is also performed to quantify the R_s and R_{ct} are shown in Figure 12d. The R_{ct} value of the SSC device demonstrates low (40 Ω) value, that is attributed to high surface area along with high conductivity of the NCO/GQDs-10% electrode. Moreover, the impedance behavior of SSC devices is similar to that of ASC devices, but marginal decrement can be observed in the R_{ct} values and equivalent series resistance endures their higher conductivity and low ion diffusion on resistance of SSC devices over ASC device. The energy density (E) and power density (P) of SSC device is estimated using GCD curves at different current densities by using the equation as like ASC device. The SSC device exhibited high energy density (E) of 24.30 Wh kg^{-1} and maximum power density (P) of 500 W kg^{-1}, respectively. The SSC device delivered specific capacitance of 175 Fg^{-1} at 1 Ag^{-1} and retained 95% (166 Fg^{-1}) capacitance retention even after 3000 cycles with an excellent coulombic efficiency of 99.58% shown in Figure 12e. The obtained energy density and power density values are better than the reported values. In the literature, only a few works were available on the NCOQDs symmetric supercapacitors. Chang et al. constructed two different symmetric supercapacitor devices with NCOQDs//NCOQDs and GNCO//GNCO. The NCOQDs//NCOQDs and GNCO//GNCO SSC device performed energy density of 5 Wh kg^{-1} at a power density of 125 W kg^{-1} and 3.9 Wh kg^{-1} at a power density of 1000 W kg^{-1}.[43] The symmetric supercapacitor (SSC) device assembled using two porous $NiCo_2O_4$ electrodes by Khalid et al. NCO//NCO exhibited energy density of 4.5 Wh kg^{-1} and maximum power density of 669.0 W kg^{-1} at the current density of 1 mA cm^{-2}. Even at higher current density of 12 mA cm^{-2}, symmetric device still delivers energy density of 2.5 Wh kg^{-1} and power density of 2532.5 W kg^{-1}.[58]

2.5. Materials' Stability–Post-Mortem Analyses

2.5.1. Post-Mortem X-ray diffraction

Understanding the materials' stability under the conditions of the supercapacitor device operation is quite important for their consideration in practical applications in addition to derive a fundamental understanding of the degradation mechanisms (if any). Therefore, we first performed the structure, phase, and morphology analyses of the electrode materials before and after cycling with a particular attention toward their functionality. XRD patterns of NCO/GQDs-10% electrode before and after cycling are shown in **Figure 13**. The XRD spectra of NCO/GQDs-10% electrode before and after cycling exhibit similar XRD pattern for all 2θ values. It can be observed that after cycling, the shape of the peaks does not change, but a slight peak position shift has been observed toward the lower 2θ angle indicating phase change. The peak shift is clearly observed at $2\theta = 36.72°$ and shown in Figure 13. At the same time, the intensities of the characteristic peaks of the NCO/GQDs-10% after cycling is slightly decreased. The NCO is easily converted as NiO, CoO, metallic (Ni and Co) quantum dots and Li_2O during lithium insertion (discharge). Which is reversible rection during charge process. The continuous conversion reactions between NiO to Ni, and between CoO to Co, accompanied by the formation and decomposition of Li_2O. Due to these continuous conversion/deconversion (lithiation/delithiation) processes the active material lost the long-range order and the crystalline metal oxide phase was gradually destroying.[94] This may cause a small decrement in the XRD peaks intensities after cycling. The quantum dots with their ultra small size don't lose their structural ordering. Moreover, the successful coating of graphene onto NCOQDs in the composite form can provide excellent mechanical stability that preserves the crystal structure even more efficiently. Hence, the NCO/GQDs-10% electrode does not show significant difference shape of the XRD patterns after cycling. There might be a possibility of phase change after plenty of cycles due to the weak structural stability of cobalt that causes intensity variation in the XRD patterns. Note that these slight structural modifications do not seem to affect the Li^+ extraction/insertion process any more since the supercapacitor capacitance fade is <0.1% per cycle.

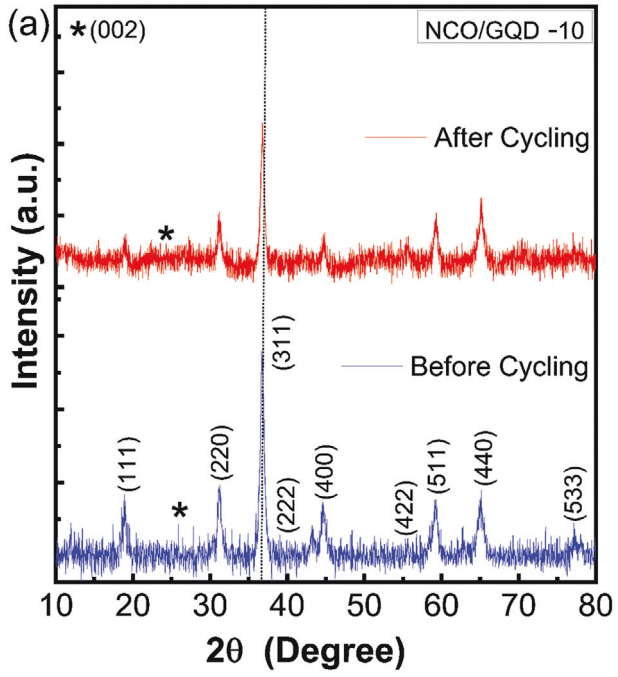

Figure 13. Post-mortem X-ray diffraction patterns of the NCO/GQDs-10% electrode. The XRD obtained are shown for NCO/GQDs-10% electrode before and after cycling.

2.5.2. Surface Morphology (After Cycling)

In addition to XRD data confirming the structural and phase stability, the SEM imaging analyses provided insights into the morphology characteristics and their stability in NCO/GQDs in supercapacitors. **Figure 14** shows post-mortem SEM images with different magnification100 nm (a), and 300 nm (b) of NCO/GQD-10% sample after 5000 cycles. The cycled NCO/GQDs-10% electrode in Figure 14a,b do not show any significant change in the particle shape but the size of the grains were increased after cycling comparing to before cycling sample (as shown in the Figure 14a,b) may be due to the volume expansion nature of Co metal in the NCO. They displayed pores on the surface and some particulates were agglomerated after cycling that can be caused by an increase in the internal temperature after several charge–discharge cycles. But we do not find any cracks and breaks among the particles or upon the particles after several cycles. That represents the uniqueness of the graphenized NCOQDs. The quantum dots will have enormous surface to volume ratio and facilitate the mechanical strength that prevents the structural integrity and graphene sheets enhance the compactness and more stability. These special features avoid the peel of the material during charging–discharging leading to high capacitance to the electrode.

3. Conclusion

In this work, NCO quantum dots and their composites were synthesized by hydrothermal method and their applicability in asymmetric and symmetric supercapacitor applications is evaluated. A thorough investigation conducted on the production, description, and assessment of the electrochemical performance of highly functional NCO/GQDs in supercapacitors indicate that these NCO/GQDs provide increased energy efficiency. A comprehensive investigation conducted into the impact of varying GQD amounts on the energy performance characteristics of NCO/GQDs in supercapacitors allowed us to optimize the specific composition to derive enhanced energy efficiency characteristics in both symmetric and asymmetric supercapacitors. Comprehensive structural and chemical bonding tests, utilizing Raman spectroscopy measurements and X-ray diffraction (XRD), reveal that all NCO/GQD composites crystallize in the spinel cubic phase of $NiCo_2O_4$, with graphene integration visible in each and every NCO/GQDs electrode materials. The electron microscopy analyses revealed uniformly distributed spherical particles with a size distribution between 5 and 9 nm, confirming the generation of QDs. Under optimum conditions, the NCO/GQDs composite electrodes deliver superior specific capacitances in the range 3940–1900 Fg^{-1} at a current density of 0.5 Ag^{-1} with excellent structural stability, which are higher values than that of pristine NCO (1964 Fg^{-1} @ 0.5 Ag^{-1}). Among all electrodes, NCO/GQDs −10% shows the best specific capacitance of 3940 Fg^{-1} at current density of 0.5 Ag^{-1} and retained 98% of capacitance even after 5000 cycles. Moreover, the NCO/GQDs-10%//AC asymmetric supercapacitor demonstrated excellent energy density of 118.04 Wh kg^{-1} and power density of 798 W kg^{-1} with an extraordinary coulombic efficiency of 99.05% after 3000 cycles. The NCO/GQDs −10%//NCO/GQDs −10% symmetric supercapacitor showed high energy density of 24.03 Wh kg^{-1} and power density of 500 W kg^{-1} with an excellent coulombic efficiency of 99.58% after 3000 cycles. The NCO/GQDs-10% nanocomposite exhibited remarkable electrochemical performance, making it a viable electrode for ASC and SSC devices. Its long cycle stability and high specific capacitance are characteristics sought for use in high power supercapacitors. Furthermore, the fundamental and mechanistic aspects of these materials under the cycling and functionality in supercapacitor indicate that there are no significant changes in terms of their structure, phase, and morphology. The structure and chemistry of the NCO/GQDs under cycling conditions favors their applicability in both asymmetric and symmetric supercapacitors. Therefore, in addition to being applicable to a large class of compounds based on quantum dots integrating graphene, the results of the present work will provide a strong foundation step toward the future energy device technology based on quantum dots.

4. Experimental Section

Materials: The chemicals used were $NiSO_4.6H_2O$ (nickel sulphate hexahydrate, purity, 99.7%), $CoSO_4.7H_2O$ (cobalt sulphate heptahydrate, purity 99.99%), $C_6H_8O_7$ (citric acid, purity 99.9%), CH_4N_2O (urea, nanopowders, purity 99.5%). All the chemicals were purchased from Sigma–Aldrich and were of analytical grade in good working condition and used without further purification. All chemical solutions were prepared using a Milli-Q water purification system (Milli-Q, USA).

Preparation of $NiCo_2O_4$/Graphene Quantum Dots (NCO/GQDs): The synthesis approach adopted in this work is schematically presented in **Figure 15**. GQDs were synthesized using citric acid (CA) by bottom-up method. In the bottom-up method different weight percent (5%,10%, and 15%) of CA was taken into a glass beaker (50 mL) and heated at 200 °C

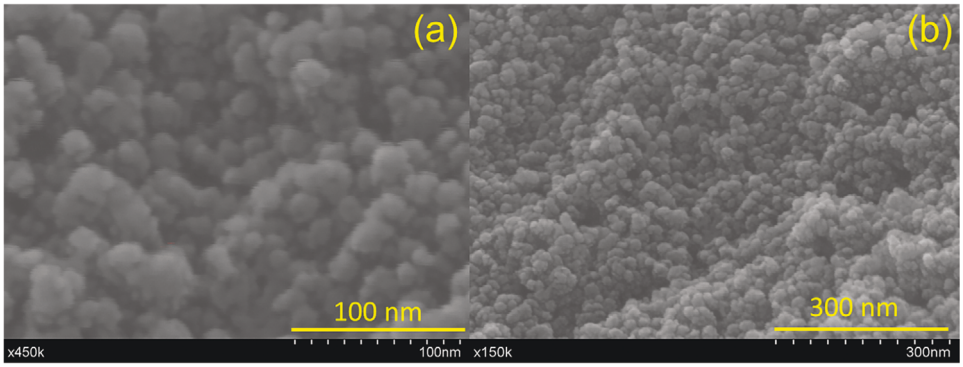

Figure 14. Post -mortem FE-SEM images of NCO/GQDs-10% electrode after 5000 cycles at 100 nm magnification (a), and 300 nm magnification (b), respectively.

for 20 min. the orange color liquid was formed from CA, after heating-on-heating mantle. Then the orange color liquid can cool down to room temperature. After that, a 100 mL of 100 mg mL^{-1} NaOH solution was added into the orange-colored liquid dropwise with continuous vigorous stirring and GQDs were prepared successfully. Citric acid contains three carboxylic acid (—COOH) functional groups. The chemical reactions take place among the precursor molecules to form a graphitic core inside the GQD system.[95] In a typical synthesis process of NCO/GQDs composites different amounts 5, 10, and 15 g of GQDs orange liquid were added 50 mL DI water and these were called as GQDs 5%, 10%, and 15% respectively. $NiCo_2O_4$ (NCO) and $NiCo_2O_4$/GQDs (NCO/GQDs) were synthesized using simple hydrothermal method. In a typical synthesis 1.05 g of Nickel sulphate hexahydrate ($NiSO_4$. 6 H_2O), 2.25 g of cobalt sulphate heptahydrate ($CoSo_4$.7 H_2O) and 3.6 g urea (CH_4N_2O) were dissolved in 50 mL of DI water and stirred for 20 min for preparation of homogeneous solution. Later different amounts (wt%) of 5%, 10%, and 15% GQDs were added to this mixer then continuously stirring for another 30 min until the solute was completely dissolved and formed as homogenous solution. Each mixed solution was transferred to a 100 mL Teflon lined stainless steel auto clave and heated 180 °C for 24 h. During synthesis, Co^+ and Ni^+ cations react with the carboxylic acid (-COOH) functional group of GQDs. The hydrolysis products of urea also help to strengthen the bonding/interface of Co^+ and Ni^+ cations with GQDs to form bimetallic NCO/GQDs composite.[96] With increasing GQDs concentration, the binding/interface nature of —COOH with NCO is increased and a strong interface is formed between NCO and GQDs in NCO/GQDs nanocomposite. In addition to carbon content in GQDs, the functional groups of carbon in the urea also affect the tuning of the quantum dots.[97] After the auto clave was cooled down to room temperature the precipitate was obtained. This precipitate was washed with Ethanol and DI water several times then subjected to centrifugation at 10 000 rpm 10 min to remove the reagents. Later this centrifuged product was dried at 80 °C for 12 h in an oven. Then, this product was calcined at 400 °C for 3 h in air atmosphere to obtain final sample. The graphene quantum dots were synthesized from citric acid that was most responsible for growth and tuning the morphology for NCO/GQDs composites. In the presence of inorganic substances, the crystal growth of NCO can be retorted. Moreover, the great absorbability and amorphous nature of carbon easily tunes the particles size and morphology. After inculcation of GQDs into NCO framework, the crystallite size and morphology can be significantly reduced. Hence, GQDs are more responsible for growth and tuning the morphology. The final products were named as NCO/GQDs-5%, NCO/GQDs-10%, and NCO/GQDs-15%, respectively. The obtained final product collected for subsequent characterization. In this synthesis method without adding GQDs we prepared pure $NiCo_2O_4$ sample.

Materials Characterization: Crystallography and phase of as synthesized samples were analyzed by X- ray diffraction (XRD) with a diffractometer Rigaku, model 2500 pc using the Cu K_λ radiation (λ = 0.15 406 nm) as the X- ray source. XRD data were collected in the 2θ range 10°–80° at a scanning rate of 0.03 min^{-1}. Raman scattering (RS) spectra were collected with a confocal micro-Raman spectrometer at room temperature Horiba Jobin – Yuon HR 800 UV in the range of 100–2000 cm^{-1} at a spectral resolution of 1 cm^{-1} using Nd – YAG laser excitation source (λ = 532 nm) with the back scattering mode. The surface morphology and the particle size were characterized by field emission scanning electron microscopy (FE – SEM) using HITACHI 4700 microscope. To improve the conductivity of powder samples an ultrathin gold layer was deposited for 5 min on to the surface of the sample by rf – Magnetron sputtering (E – 1030 ion sputter, Hitachi, Japan). The phase identification and the microstructure of the samples were characterized by high resolution transition electron

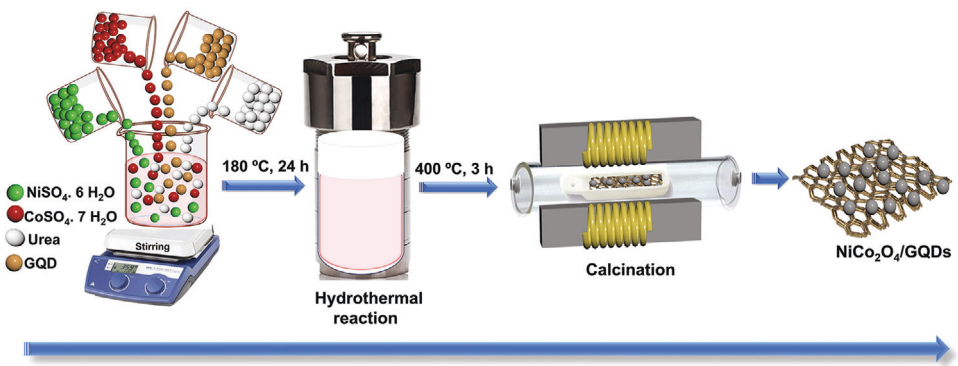

Figure 15. Schematic diagram of the synthesis approach & steps involved in the synthesis of NCO QDs and NCO/GQDs.

microscopy (HRTEM) and selected area electron (SAE) diffraction by a HRTEM – FEI microscope (TECHNAI G^2 – 30 S – twin D 905) at an accelerating voltage of 200 KV. The surface area and pore diameter/volume of the samples were measured by atomic surface analyzer (3 – Flex, Micrometrics) using Brunauer–Emmett–Teller (BET) and Barrett–Joyner–Halenda (BJH) calculation. The surface properties and chemical composition of the synthesized samples were characterized by X- ray photoelectron spectroscopy (XPS) K_α Thermo scientific) using a monochromatic A1 K_α X- ray radiation (1486.6 eV). The obtained data were collected and processed using the marketed software CASA XPS. The elemental composition of the samples was examined by an energy dispersive X- ray analysis (EDS) instrument attached to FE SEM apparatus.

Electrochemical Properties and Performance Evaluation: Electrochemical properties of the synthesized samples were investigated using a three – electrode aqueous cell using the NCOQDs and NCO/GQDs composites as the working electrode. A platinum metal strip as counter electrode and Ag/AgCl was used as a reference electrode. The working electrode was prepared with a mixture of 90 wt% NCO/GQDs composites and 10 wt% polyvinylidine fluoride (PVDF) dissolved in NMP (N – methyl – 2pyrrolidone) to from a slurry spread on Ni metal (1 × 0.5 cm^2) substrate. A 10 wt% carbon acetylene black was added in the preparation of pure NCO-QDs electrode. The active working area of the electrode is 1 × 0.5 cm^2 contains 2–3 mg of slurry that dried at 100 °C for 5 h to reduce impurity traces. A 1 mol L^{-1} Li_2SO_4 aqueous solution was used as electrolyte. The electrochemical measurements were conducted using an electrochemical workstation model solartron in the potential cut-off 0.0–0.6 V. Electrochemical impedance spectroscopy (EIS) was carried out using in the frequency range 1 Hz–1 MHz using a voltage bias of 5 mV at the cell fully charged state. Multiple measurements were made on a set of at least three samples for every composition. The results showed that the relative standard deviation (RSD) of the measurements was ≈ 2%, indicating that the stability of cells was satisfactory.

Asymmetric Supercapacitors (ASC) & Symmetric Supercapacitors (SSC) – Fabrication and Performance Evaluation: To evaluate the practical applications of synthesized NCO/GQDs-10% electrode for energy storage rechargeable asymmetric supercapacitor (ASC) configuration was constructed using two electrode pouch type devices, which was fabricated by sandwiching (whatman) filter paper as a separator between two electrodes immersed in PVA/KOH gel. The NCO/GQDs-10% electrode is used as positive electrode whereas activated carbon (AC) is used as negative electrode, a PVA/KOH gel electrolyte was used as an ion-conductive channel, a whatman filter used as a separator to prevent direct contact. In the preparation of gel electrolyte, 1 g of PVA was dissolved in 60 mL of DI water and subjected to heating at 80 °C. 10 g of potassium hydroxide (KOH) pellets was added to the solution during the stirring then a transparent gel-type solution can be achieved. The NCO/GQDs-10% electrode with AC electrode is expected to spread operational working voltage window range of ASC device is determined as 1.6 V. whereas >1.6 V, the oxygen evolution reactions can be observed due to polarization between electrodes. The mass ratio between negative and positive electrode is determined by balancing the charge stored in each electrode according to the following Equation (8):

$$\frac{m^+}{m^-} = \frac{C^- \times \Delta V^-}{C^+ \times \Delta V^+} \tag{8}$$

where m^+ and m^- are the mass loadings of positive (NCO/GQDs-10%) and negative electrode (AC) deposited on the Ni foil current collector. C^+ and C^- stands for the specific capacitance of the positive and negative electrodes and ΔV^+ and ΔV^- represents the potential window of positive and negative electrodes, respectively. The mass load between negative and positive electrodes to be maintained as 4. The aqueous based electrolytes are used to minimize the cost of the materials especially for electrolyte. Asymmetric supercapacitors are explored using aqueous electrolyte in which (EDLC) carbon-based materials can be used as negative electrode. Whereas Faradaic transition metal oxide/hydroxide/sulphide materials can be used as positive electrode materials, respectively. The higher operational potential window, high energy density and high-power density could be possible to achieve in ASCs. The formula for calculating the specific capacitance (C_s, Fg^{-1}), energy density (E, $Wh\,kg^{-1}$) and power density (P, $W\,kg^{-1}$) of the ASC device are given below as Equations (9)–(11):

$$C_s = \frac{I \times \Delta t}{m \times \Delta V} (F\,g^{-1}) \tag{9}$$

$$E = \frac{c_s \times (\Delta V)^2}{2 \times 3.6} (Wh\,kg^{-1}) \tag{10}$$

$$P = \frac{E \times 3600}{\Delta t} (W\,kg^{-1}) \tag{11}$$

where "I" is the discharge current (A), "m" is the weight of the active material, "Δt" is the discharge time (sec), "ΔV" is the potential window. The SSC was constructed with similar electrodes. The symmetric device is fabricated with two electrodes that were assembled using similar NCO-GQDs-10% electrodes. The symmetric device of NCO/GQDs-10% was fabricated in the same way as that used for asymmetric device. To study the reproducibility of the electrochemical tests, three batches of cells (both ASC and SSC) were tested in parallel with the same percentage of NCOGQDs-10% content. The results showed that the relative standard deviation (RSD) of the measurements was ≈ 2%, indicating that the stability of cells was satisfactory.

Supporting Information

Supporting Information is available from the Wiley Online Library or from the author.

Acknowledgements

The authors also acknowledge, with pleasure, support from the National Science Foundation (NSF) with NSF-PREM grant #DMR-1827745. A portion of this research was performed on a project award (10.46936/cpcy.proj.2021.60259/60008213) from the Environmental Molecular Sciences Laboratory, a DOE Office of Science User Facility sponsored by the Biological and Environmental Research program under Contract No. DE-AC05-76RL01830 and also funded in part by a grant from the Washington State Department of Commerce's Clean Energy Fund. A portion of research was supported by the UTEP-PNNL Laboratory Directed Research and Development (LDRD) initiative at Pacific Northwest National Laboratory (PNNL). The UTEP-PNNL joint activities in the topical area of advanced materials and energy technologies are greatly appreciated by the authors. Finally, the authors sincerely thank Dr. Debabrata Das for his involvement in helpful discussions and technical assistance when needed.

Conflict of Interest

The authors declare no conflict of interest.

Data Availability Statement

The data that support the findings of this study are available from the corresponding author upon reasonable request.

Keywords

asymmetric supercapacitor (ASC), energy storage, hydrothermal synthesis, $NiCo_2O_4$/graphene quantum dots (NCO/GQDs), symmetric supercapacitor (SSC), synergistic effect

Received: January 25, 2024
Revised: March 26, 2024
Published online:

[1] N. Li, R. Guo, W. Chen, V. Körstgens, J. E. Heger, S. Liang, C. J. Brett, M. A. Hossain, J. Zheng, P. S. Deimel, A. Buyruk, F. Allegretti, M. Schwartzkopf, J. G. C. Veinot, G. Schmitz, J. V. Barth, T. Ameri, S. V. Roth, P. Müller-Buschbaum, *Adv. Funct. Mater.* **2021**, *31*, 2102105.
[2] X. Liu, Y. Li, L. Zeng, X. Li, N. Chen, S. Bai, H. He, Q. Wang, C. Zhang, *Adv. Mater.* **2022**, *34*, 2108327.
[3] Y. Zhai, B. Zhang, R. Shi, S. Zhang, Y. Liu, B. Wang, K. Zhang, G. I. N. Waterhouse, T. Zhang, S. Lu, *Adv. Energy Mater.* **2022**, *12*, 2103426.
[4] F. Wang, J. Lee, L. Chen, G. Zhang, S. He, J. Han, J. Ahn, J. Y. Cheong, S. Jiang, I.-D. Kim, *ACS Nano* **2023**, *17*, 8866.
[5] A. D. Marinov, L. Bravo Priegue, A. R. Shah, T. S. Miller, C. A. Howard, G. Hinds, P. R. Shearing, P. L. Cullen, D. J. L. Brett, *ACS Nano* **2023**, *17*, 5163.
[6] G. Wu, X. Wu, X. Zhu, J. Xu, N. Bao, *ACS Nano* **2022**, *16*, 10130.
[7] R. Ma, X. Zhang, J. Zhuo, L. Cao, Y. Song, Y. Yin, X. Wang, G. Yang, F. Yi, *ACS Nano* **2022**, *16*, 9713.
[8] F. Zheng, C. Li, Z. Li, X. Cao, H. Luo, J. Liang, X. Zhao, J. Kong, *Small* **2023**, *19*, 2206355.
[9] M. Wang, S. Feng, C. Bai, K. Ji, J. Zhang, S. Wang, Y. Lu, D. Kong, *Small* **2023**, *19*, 2300386.
[10] C. Xiong, Y. Zhang, Y. Ni, *J. Power Sources* **2023**, *560*, 232698.
[11] M. A. del Valle, M. A. Gacitúa, F. Hernández, M. Luengo, L. A. Hernández, *Polymers* **2023**, *15*, 1450.
[12] M. A. del Valle, R. Salgado, F. Armijo, *J. Electrochem. Sci.* **2014**, *9*, 1557.
[13] Z. Xu, Z. Zhang, H. Yin, S. Hou, H. Lin, J. Zhou, S. Zhuo, *RSC Adv* **2020**, *10*, 3122.
[14] G. Qu, Z. Wang, X. Zhang, S. Zhao, C. Wang, G. Zhao, P. Hou, X. Xu, *Chem. Eng. J.* **2022**, *429*, 132406.
[15] P. Siwatch, K. Sharma, S. K. Tripathi, *Electrochim. Acta* **2020**, *329*, 135084.
[16] E. Umeshbabu, G. Rajeshkhanna, G. R. Rao, *Int. J. Hydrog. Energy* **2014**, *39*, 15627.
[17] B. K. Singh, D. Das, N. Attarzadeh, S. N. Chintalapalle, C. V. Ramana, *Nano Select* **2023**, *4*, 145.
[18] B. K. Singh, D. Das, C. Gonzalez, C. V. Ramana, *Energy Technol* **2023**, *11*, 2300360.
[19] Y. Yan, Y. Liu, W. Ni, J. Wu, M. Liu, T. Liu, *ChemNanoMat* **2016**, *2*, 1077.
[20] Z. Wu, Y. Zhu, X. Ji, *J. Mater. Chem. A* **2014**, *2*, 14759.
[21] T. Zhao, C. Liu, T. Meng, W. Deng, L. Zheng, F. Yi, A. Gao, D. Shu, *Small* **2022**, *18*, 2201286.
[22] P. Nayak, M. Sahoo, S. K. Nayak, *Ceram. Int.* **2020**, *46*, 3818.
[23] X. Shi, S. L. Bernasek, A. Selloni, *J. Phys. Chem. C* **2016**, *120*, 14892.
[24] H. S. AlSalem, K. M. S. Katubi, M. S. Binkadem, S. T. Al-Goul, A. M. Wahba, *ACS Omega* **2023**, *8*, 40808.
[25] D. Kong, W. Ren, C. Cheng, Y. Wang, Z. Huang, H. Y. Yang, *ACS Appl. Mater. Interfaces* **2015**, *7*, 21334.
[26] A. L. Narayana, G. Venkataprasad, S. Praveen, C. W. Ho, H. K. Kim, T. M. Reddy, C. M. Julien, C. W. Lee, *Sens. Actuator A Phys.* **2022**, *341*, 113555.
[27] P. R. Kharangarh, N. M. Ravindra, R. Rawal, A. Singh, V. Gupta, *J. Alloys Compd.* **2021**, *876*, 159990.
[28] V. Gayathri, I. J Peter, K. Ramachandran, S. Karazhanov, C. Raja Mohan, *Energy & Fuels* **2021**, *35*, 13360.
[29] A. S. Rasal, S. Yadav, A. Yadav, A. A. Kashale, S. T. Manjunatha, A. Altaee, J.-Y. Chang, *ACS Appl. Nano Mater.* **2021**, *4*, 6515.
[30] W. Jia, H. Wu, Z. Liu, G. Cai, J. Wen, G. Hu, T. Tang, X. Li, M. Li, H. Huang, *ACS Appl. Nano Mater.* **2022**, *5*, 17795.
[31] Y. Huang, T. Shi, Y. Zhong, S. Cheng, S. Jiang, C. Chen, G. Liao, Z. Tang, *Electrochim. Acta* **2018**, *269*, 45.
[32] Y. Zhu, Z. Wu, M. Jing, H. Hou, Y. Yang, Y. Zhang, X. Yang, W. Song, X. Jia, X. Ji, *J. Mater. Chem. A* **2015**, *3*, 866.
[33] P. Siwatch, K. Sharma, N. Singh, N. Manyani, S. K. Tripathi, *Electrochim. Acta* **2021**, *381*, 138235.
[34] X. Yin, C. Zhi, W. Sun, L.-P. Lv, Y. Wang, *J. Mater. Chem. A* **2019**, *7*, 7800.
[35] S. Zhang, L. Sui, H. Dong, W. He, L. Dong, L. Yu, *ACS Appl. Mater. Interfaces* **2018**, *10*, 12983.
[36] P. S. Shewale, K.-S. Yun, *Nanomaterials* **2021**, *11*, 852.
[37] D. Li, Y. Gong, Y. Zhang, C. Luo, W. Li, Q. Fu, C. Pan, *Sci. Rep.* **2015**, *5*, 12903.
[38] N. V. Nguyen, T. V. Tran, S. T. Luong, T. M. Pham, K. V. Nguyen, T. D. Vu, H. S. Nguyen, N. V. To, *ChemistrySelect* **2020**, *5*, 7060.
[39] S. Sun, S. Wang, S. Li, Y. Li, Y. Zhang, J. Chen, Z. Zhang, S. Fang, P. Wang, *J. Mater. Chem. A* **2016**, *4*, 18646.
[40] A. G. El-Deen, M. H El-Shafei, A. Hessein, A. H. Hassanin, N. M. Shaalan, A. A. El-Moneim, *Nanotechnology* **2020**, *31*, 365404.
[41] H. Jiang, K. Yang, P. Ye, Q. Huang, L. Wang, S. Li, *RSC Adv.* **2018**, *8*, 37550.
[42] J. Luo, J. Wang, S. Liu, W. Wu, T. Jia, Z. Yang, S. Mu, Y. Huang, *Carbon* **2019**, *146*, 1.
[43] H.-W. Chang, J.-X. Fu, Y.-C. Huang, Y.-R. Lu, C.-H. Kuo, J.-L. Chen, C.-L. Chen, J.-F. Lee, J.-M. Chen, Y.-C. Tsai, W. Ching Chou, C.-L. Dong, *Catal. Today* **2020**, *348*, 290.
[44] H.-C. Chien, W.-Y. Cheng, Y.-H. Wang, T.-Y. Wei, S.-Y. Lu, *J. Mater. Chem.* **2011**, *21*, 18180.
[45] J. Xiao, S. Yang, *J. Mater. Chem.* **2012**, *22*, 12253.
[46] C. Yuan, J. Li, L. Hou, X. Zhang, L. Shen, X. W. Lou, *Adv. Funct. Mater.* **2012**, *22*, 4592.
[47] A. Lakshmi-Narayana, M. Dhananjaya, N. Guru-Prakash, O. M. Hussain, A. Mauger, C. M. Julien, *ChemistrySelect* **2018**, *3*, 9150.
[48] Z.-Q. Liu, H. Cheng, N. Li, T. Y. Ma, Y.-Z. Su, *Adv. Mater.* **2016**, *28*, 3777.
[49] C. V. Ramana, M. Massot, C. M. Julien, *Surf. Interface Anal.* **2005**, *37*, 412.
[50] A. N. Nair, M. F. Sanad, R. Jayan, G. Gutierrez, Y. Ge, M. M. Islam, J. A. Hernandez-Viezcas, V. Zade, S. Tripathi, V. Shutthanandan, C. V. Ramana, S. T. Sreenivasan, *Small* **2022**, *18*, 2202648.
[51] N. Attarzadeh, D. Das, S. N. Chintalapalle, S. Tan, V. Shutthanandan, C. V. Ramana, *ACS Appl. Mater. Interfaces* **2023**, *15*, 22036.
[52] C. Y. Foo, H. N. Lim, M. A. b. Mahdi, K. F. Chong, N. M. Huang, *J. Phys. Chem. C* **2016**, *120*, 21202.
[53] A. Lakshmi-Narayana, K. Sivajee-Ganesh, M. Dhananjaya, A. Narayan-Banerjee, C. M. Julien, S.-W. Joo, *Batteries* **2022**, *8*, 149.
[54] S. Abdolhosseinzadeh, H. Asgharzadeh, H. Seop Kim, *Sci. Rep.* **2015**, *5*, 10160.
[55] Y. Bai, M. Liu, J. Sun, L. Gao, *Ionics* **2016**, *22*, 535.
[56] A. Lakshmi-Narayana, M. Dhananjaya, C. M. Julien, S. W. Joo, C. V. Ramana, *ACS Appl. Mater. Interfaces* **2023**, *15*, 20925.
[57] X. Sun, J. Sun, L. Guo, L. Hou, C. Yuan, *RSC Adv.* **2020**, *10*, 35611.
[58] S. Khalid, C. Cao, L. Wang, Y. Zhu, *Sci. Rep.* **2016**, *6*, 22699.
[59] S. Sahoo, J.-J. Shim, *ACS Sustain. Chem. Eng.* **2017**, *5*, 241.
[60] B. Sachin Kumar, V. C. Gudla, R. Ambat, S. K. Kalpathy, S. Anandhan, *J. Inorg. Organomet. Polym. Mater.* **2018**, *28*, 1885.
[61] A. Lakshmi-Narayana, L. Zhang, C. Jiao, C. M. Julien, Y. Qiu, *Ceram. Int.* **2020**, *46*, 10299.
[62] S. Sun, S. Li, S. Wang, Y. Li, L. Han, H. Kong, P. Wang, *Mater. Lett.* **2016**, *182*, 23.
[63] X.-H. Guan, M. Li, H.-Z. Zhang, L. Yang, G.-S. Wang, *RSC Adv.* **2018**, *8*, 16902.
[64] M. Naushad, T. Ahamad, M. Ubaidullah, J. Ahmed, A. A. Ghafar, K. M. Al-Sheetan, P. Arunachalam, *J. King Saud Univ. Sci.* **2021**, *33*, 101252.
[65] C. Yao, Y. Su, Y. Li, J. Li, *Int. J. Electrochem. Sci.* **2021**, *16*, 150917.
[66] D. Yan, H. Zhang, S. Li, G. Zhu, Z. Wang, H. Xu, A. Yu, *J. Alloys Compd.* **2014**, *607*, 245.
[67] Y. Zheng, Z. Lin, W. Chen, B. Liang, H. Du, R. Yang, X. He, Z. Tang, X. Gui, *J. Mater. Chem. A* **2017**, *5*, 5886.

[68] C. V. Ramana, S. Roy, V. Zade, A. K. Battu, N. Makeswaran, V. Shutthanandan, *J. Phys. Chem. Solids* **2021**, *157*, 110174.
[69] J. F. Moulder, W. F. Stickle, P. E. Sobol, K. D. Bomben, *Handbook of X-Ray Photoelectron Spectroscopy, Physical Electronics Division, Perkin-Elmer Corporation*, Eden Prairie, MN, USA, **1992**.
[70] A. P. Grosvenor, M. C. Biesinger, R. S. C. Smart, N. S. McIntyre, *Surf Sci.* **2006**, *600*, 1771.
[71] M. C. Biesinger, B. P. Payne, L. W. M. Lau, A. Gerson, R. S. C. Smart, *Surf. Interface Anal.* **2009**, *41*, 324.
[72] A. P. Grosvenor, S. D. Wik, R. G. Cavell, A. Mar, *Inorg. Chem.* **2005**, *44*, 8988.
[73] R. Ding, L. Qi, M. Jia, H. Wang, *Nanoscale* **2014**, *6*, 1369.
[74] C. Qiu, L. Jiang, Y. Gao, L. Sheng, *Mater. Des.* **2023**, *230*, 111952.
[75] R. Al-Gaashani, A. Najjar, Y. Zakaria, S. Mansour, M. A. Atieh, *Ceram. Int.* **2019**, *45*, 14439.
[76] Z. Gao, W. Yang, J. Wang, N. Song, X. Li, *Nano Energy* **2015**, *13*, 306.
[77] J. Yang, H. Liu, W. N. Martens, R. L. Frost, *J. Phys. Chem. C* **2010**, *114*, 111.
[78] M. C. Biesinger, B. P. Payne, A. P. Grosvenor, L. W. M. Lau, A. R. Gerson, R. S. C. Smart, *Appl. Surf. Sci.* **2011**, *257*, 2717.
[79] S. Wang, S. Sun, S. Li, F. Gong, Y. Li, Q. Wu, P. Song, S. Fang, P. Wang, *Dalton Trans* **2016**, *45*, 7469.
[80] J. Zhao, Z. Li, X. Yuan, Z. Yang, M. Zhang, A. Meng, Q. Li, *Adv. Energy Mater.* **2018**, *8*, 1702787.
[81] A. Lakshmi-Narayana, M. Dhananjaya, N. Guru-Prakash, A. Mauger, C. M. Julien, O. M. Hussain, *Heliyon* **2019**, *5*, e02060.
[82] A. Lakshmi Narayana, M. Dhananjaya, N. Guru Prakash, O. M. Hussain, C. M. Julien, *Ionics* **2017**, *23*, 3419.
[83] K. Vijaya Sankar, S. Surendran, K. Pandi, A. M. Allin, V. D. Nithya, Y. S. Lee, R. K Selvan, *RSC Advances* **2015**, *5*, 27649.
[84] S. K. Gaikwad, S. P. Kharat, K. Haritha, Y. D. Kolekar, C. V. Ramana, *Inorg. Chem.* **2023**, *62*, 11837.
[85] M. Satish, H. M. Shashanka, S. Saha, K. Haritha, D. Das, P. N. Anantharamaiah, C. V. Ramana, *ACS Appl. Mater. Interfaces* **2023**, *15*, 15691.
[86] D. Zhang, H. Yan, Y. Lu, K. Qiu, C. Wang, C. Tang, Y. Zhang, C. Cheng, Y. Luo, *Nanoscale Res. Lett.* **2014**, *9*, 139.
[87] G. He, L. Wang, H. Chen, X. Sun, X. Wang, *Mater. Lett.* **2013**, *98*, 164.
[88] X. Wang, A. Sumboja, M. Lin, J. Yan, P. S. Lee, *Nanoscale* **2012**, *4*, 7266.
[89] S. K. Meher, G. R. Rao, *J. Power Sources* **2012**, *215*, 317.
[90] A. Singh, A. K. Ojha, *J. Colloid Interface Sci.* **2020**, *580*, 720.
[91] X. Li, L. Jiang, C. Zhou, J. Liu, H. Zeng, *NPG Asia Mater* **2015**, *7*, e165.
[92] W. Chu, Z. Shi, Y. Hou, D. Ma, X. Bai, Y. Gao, N. Yang, *ACS Appl. Mater. Interfaces* **2020**, *12*, 2763.
[93] J. Yang, W. Liu, H. Niu, K. Cheng, K. Ye, K. Zhu, G. Wang, D. Cao, J. Yan, *Nano Res* **2018**, *11*, 4744.
[94] M. Islam, G. Ali, M.-G. Jeong, K. Y. Chung, K.-W. Nam, H.-G. Jung, *Int. J. Energy Res.* **2021**, *45*, 15036.
[95] S. A. Ansari, *Nanomaterials* **2022**, *12*, 3814.
[96] H. Ma, J. He, D. B. Xiong, J. Wu, Q. Li, V. Dravid, Y. Zhao, *ACS Appl. Mater. Interfaces* **2016**, *8*, 1992.
[97] Z. H. Ibupoto, S. Elhag, M. S. AlSalhi, O. M. Nur, *Electroanalysis* **2014**, *8*, 1773.